

Highlights

An Entropy-Stable/Double-Flux scheme for the multi-component compressible Navier-Stokes equations

Vahid Badrkhani, T. Jeremy P. Karpowski, Christian Hasse

- We introduce an Entropy-Stable/Double-Flux approach for solving multi-component compressible Navier–Stokes equations.
- To enhance stability, we have coupled an Entropy-Stable approach with the Double-Flux method. With a suitable choice of numerical flux, the scheme ensures entropy stability and satisfies the second law of thermodynamics in an integral sense.
- Compared to conventional numerical fluxes, the Entropy-Stable/Double-Flux schemes offer superior stability, robustness, and oscillation-free behavior for multi-component compressible Navier–Stokes simulations.
- We have developed a novel hybrid dissipation method by blending a standard hybrid dissipation term with the Entropy-Stable/Double-Flux algorithm.
- The proposed numerical flux is rigorously verified and validated through extensive multi-dimensional benchmark tests and complex multi-component compressible flow problems.

An Entropy-Stable/Double-Flux scheme for the multi-component compressible Navier-Stokes equations

Vahid Badrkhani^{a,b,*}, T. Jeremy P. Karpowski^a, Christian Hasse^a

^a*Institute for Simulation of Reactive Thermo-Fluid Systems, Technical University of Darmstadt, Germany*

^b*Institute for Mechanics, Computational Mechanics Group, Technical University of Darmstadt, Germany*

Abstract

We present a novel combination of numerical techniques to improve the efficiency, accuracy, and robustness of multi-component compressible flow simulations. At the core of our approach is an Entropy-Stable formulation that preserves kinetic energy and integrates a Double-Flux scheme tailored for multi-component flows with variable specific heat ratios. This formulation yields low-dissipation, oscillation-free solutions and enhances stability compared to standard fully conservative methods. To further improve robustness, we introduce a new hybrid dissipation strategy that blends the Entropy-Stable/Double-Flux approach with conventional dissipation mechanisms. We provide a rigorous proof that the resulting numerical flux satisfies a semi-discrete entropy inequality, ensuring consistency with the second law of thermodynamics. For time integration, we employ an explicit Runge–Kutta scheme in combination with adaptive mesh refinement to capture local flow features dynamically. The method is implemented within an existing compressible Navier–Stokes solver based on OpenFOAM. Benchmark cases, including multi-dimensional interface and shock-interface interactions, demonstrate the effectiveness of the proposed framework. The results confirm its favorable stability and robustness, validating the approach as a promising advancement for high-fidelity simulations of supersonic flows.

Keywords: Entropy-Stable schemes, Double-Flux method, multi-component compressible flow, finite-volume methods, supersonic flow simulation.

1. Introduction

The accurate and robust simulation of multi-component compressible flows with material interfaces is crucial for numerous engineering applications, such as combustion in propulsion systems and explosive detonation products, as well as scientific studies involving flow instabilities, chemical reactions, and phase transitions. These complex flows often feature

*Corresponding author

Email addresses: `badrkhani@stfs.tu-darmstadt.de` (Vahid Badrkhani), `karpowski@stfs.tu-darmstadt.de` (T. Jeremy P. Karpowski), `hasse@stfs.tu-darmstadt.de` (Christian Hasse)

nonlinear wave interactions, including shock and rarefaction waves, contact discontinuities, and material interfaces between different fluids. To capture these intricate phenomena, interface-capturing methods have been extensively studied. Various numerical approaches have been proposed, including finite difference methods [1, 2, 3], finite volume schemes [4, 5, 6, 7], and discontinuous Galerkin methods [8, 9, 10, 11], among others.

Tadmor’s pioneering work on Entropy-Conservative (EC) numerical fluxes [12, 13] laid the foundation for developing schemes that ensure compliance with the entropy condition, thereby aligning with the second law of thermodynamics. These EC fluxes, when combined with dissipation terms using entropy variables, result in numerical schemes that inherently produce entropy correctly. Chandrasekhar [14] extended Tadmor’s concept to the compressible Euler equations, introducing an EC flux that also preserves kinetic energy in the sense articulated by Jameson [15]. This kinetic energy preservation is particularly beneficial in turbulent flow simulations, as highlighted by Subbareddy et al. [16]. Building on these ideas, more recent works by Coppola et al. [17] and Kuya et al. [18] have proposed schemes that effectively balance both kinetic energy and entropy conservation, collectively referred to as kinetic energy–and entropy-preserving schemes.

For multi-component compressible Euler equations, Entropy-Stable (ES) schemes have been formulated to respect the entropy condition [19]. However, these schemes can suffer from pressure oscillations in moving interface configurations [19] and may produce nonphysical negative densities or pressures, even at first order, in the next time step [20]. Numerical experiments have shown that while ES schemes handle shocks and stationary contact discontinuities adequately, they struggle to maintain pressure equilibrium and constant velocity in simulations involving moving interfaces [21]. A potential solution lies in the EC/ES schemes for non-conservative hyperbolic systems developed by Castro et al. [22], although non-conservative approaches come with their own set of challenges [23, 24].

Matheis and Hickel [25] conducted a comparative analysis between a fully conservative (FC) scheme and a quasi-conservative (QC) approach. Their findings revealed significantly higher temperature fields in the QC results compared to the FC scheme. Schmitt et al. [26, 27] implemented an energy correction procedure alongside an artificial viscosity method to mitigate nonphysical noise caused by steep density gradients. Terashima and Koshi [28] further refined the approach by substituting the energy conservation equation with a pressure transport equation, successfully conserving pressure equilibrium across contact interfaces.

Thermodynamic properties in multi-component flows are not constant but depend on temperature and species composition. Differences in the specific heat ratio across the material interface, induce spurious pressure oscillations [9]. Noteworthy approach for this challenge is the Double-Flux model, originally developed for calorically perfect gases by Abgrall and Karni [20] and later extended by Billet and Abgrall [29] for reacting flows. This method, which has been adapted for high-order schemes [5], has demonstrated the ability to accurately predict shock speeds, even for very strong shock waves. Ma et al. [30, 31] extended the Double-Flux method to real-gas flows and introduced an algorithm to enforce entropy stability in the numerical scheme through flux correction. However, this type of flux is not inherently Entropy-Stable, requiring entropy verification at each time step, followed by correction if necessary [32, 33].

Entropy-Stable schemes satisfy the second law of thermodynamics and effectively dampen numerical oscillations, yet they introduce spurious oscillations at material interfaces with disparate specific heat ratios. Conversely, the Double-Flux method eliminates such interfacial oscillations in multi-component flows but does not ensure thermodynamic consistency and kinetic energy preservation, rendering it unsuitable for high-speed compressible turbulent flows. Bridging these limitations — while maintaining numerical stability, thermodynamic consistency, and interfacial accuracy — remains an unresolved challenge in computational fluid dynamics.

We propose a hybrid discretization strategy that unifies Entropy-Stable and Double-Flux schemes to advance the simulation of the multi-component compressible Navier–Stokes equations. The framework ensures kinetic energy preservation, thermodynamic consistency, and robust suppression of spurious pressure oscillations at material interfaces. One key novelty is the evolution of auxiliary variables—specifically, the specific heat ratio and total enthalpy—which effectively dampens pressure artifacts typical of Entropy-Stable formulations while maintaining their theoretical rigor. This modification addresses a critical limitation in existing schemes and enhances overall numerical stability. To contextualize our contribution, Table 1 compares relevant properties—kinetic energy conservation, thermodynamic compliance, and interface robustness—across established and proposed approaches, illustrating how our method resolves key trade-offs. The proposed framework is validated through theoretical analysis and a range of benchmark test cases, demonstrating its accuracy, stability, and effectiveness in complex multi-component flow scenarios.

For clarity, we briefly distinguish between Entropy-Conservative and Entropy-Stable schemes. Entropy-Conservative methods [e.g., Tadmor, 1987] satisfy a discrete analog of thermodynamic entropy conservation for smooth solutions but may fail to control entropy growth at discontinuities. Entropy-Stable schemes, in contrast, enforce a stricter inequality ($dS/dt \geq 0$) to ensure entropy production aligns with the second law of thermodynamics, even for discontinuous flows. While both frameworks preserve fundamental physics, Entropy-Stable methods are inherently dissipative, enabling robustness in under-resolved or shocked regions.

The remainder of this paper is structured as follows: Section 2 introduces the multi-component compressible Navier-Stokes equations and discusses entropy pairs, symmetrization, and the mapping of entropy variables to conservative variables. In Section 3, we present the governing differential equations and describe the spatial and temporal discretizations used in this study, employing the finite volume method. This section focuses on the Entropy-Conservative/Stable, kinetic energy-preserving, and Double-Flux methods for simulating multi-component flows. In Section 4, we derive an Entropy-Stable/Double-Flux method, as well as a novel combined approach that accurately simulates multi-component flows with shock waves while minimizing oscillations and dissipation. Also, we mathematically prove that this method is Entropy-Stable. Section 5 presents the solver implementation used in this study, along with a discussion on adaptive mesh refinement and the computational setup. Section 6 presents the results of numerical experiments conducted using our Entropy-Stable/Double-Flux methods, compared with the standard and Double-Flux methods. These experiments include various test cases, ranging from one-dimensional to

Table 1: Table compares different models for compressible flow. The column "KE preserving" indicates whether the numerical flux follows kinetic energy-preserving schemes. The "Law of thermodynamics" column specifies whether the model satisfies the second law of thermodynamics. The column titled "Oscillation-free" indicates that the method is free of oscillations at the multi-component flow near the material interface. The symbol ★ denotes the existence of an algorithm designed to enforce entropy stability through flux correction.

Model	KE preserving	2nd Law of thermodynamics	Oscillation-free
Tadmor [12, 13]	✗	✓	✗
Jameson [15]	✓	✗	✗
Chandrashekar [14]	✓	✓	✗
Coppola et al. [17]	✓	✓	✗
Gouasmi et al. [19]	✓	✓	✗
Abgrall and Karni. [20]	✗	✗	✓
Ma et al. [30]	✗	★	✓
Current work	✓	✓	✓

three-dimensional flow scenarios. Finally, the last section provides concluding remarks.

2. Governing equations

The time-dependent, compressible Navier-Stokes equations for a multi-component gas mixture containing n chemical species can be written in the conservation law of Equation 1

$$\frac{\partial \mathbf{u}}{\partial t} + \nabla \cdot \mathbf{F}(\mathbf{u}) - \nabla \cdot \mathbf{G}(\mathbf{u}, \nabla \mathbf{u}) = \mathbf{S}, \quad (1)$$

with

$$\mathbf{u} = \begin{bmatrix} \rho Y_1 \\ \vdots \\ \rho Y_{n-1} \\ \rho \\ \rho \mathbf{v} \\ \rho E \end{bmatrix}, \mathbf{F} = \begin{bmatrix} \rho Y_1 \mathbf{v} \\ \vdots \\ \rho Y_{n-1} \mathbf{v} \\ \rho \mathbf{v} \\ \rho \mathbf{v} \otimes \mathbf{v} + p \mathbf{I} \\ (\rho E + p) \mathbf{v} \end{bmatrix}, \mathbf{G} = \begin{bmatrix} J_1 \\ \vdots \\ J_{n-1} \\ 0 \\ \tau \\ \tau \cdot \mathbf{v} - \mathbf{q} - \sum_{i=1}^n h_i J_i \end{bmatrix}, \mathbf{S} = \begin{bmatrix} \dot{\omega}_1 \\ \vdots \\ \dot{\omega}_{n-1} \\ 0 \\ 0 \\ 0 \end{bmatrix} \quad (2)$$

where $\mathbf{F}(\mathbf{u})$, $\mathbf{G}(\mathbf{u}, \nabla \mathbf{u})$ and \mathbf{S} are the inviscid, viscous flux functions and source term vector, respectively. In this context, the conservative state vector with the n_s -dimensional ($n_s = d + n + 1$, with d the number of geometrical dimensions) is $\mathbf{u} = (\rho Y_i, \rho, \rho v_j, \rho E)^T$ where ρ , v_j , Y_i , $\dot{\omega}_i$, E , p represent the density, the velocity in the j th coordinate direction, mass fraction of species i , mass production rate of chemical species i , specific total energy, and pressure, respectively. The equation of state, total energy, specific heat at constant pressure, and the

relation for the sum of species mass fractions are given by:

$$\begin{aligned}
p &= \rho R T \sum_{i=1}^n \frac{Y_i}{m_i} = \rho T \sum_{i=1}^n Y_i \frac{R}{m_i} = r \rho T \\
E &= \sum_{i=1}^n Y_i \left(e_{0i} + \int_{T_0}^T c_{pi}(T) dT \right) - \frac{p}{\rho} + \frac{|\mathbf{v}|^2}{2}, \\
c_p &= \sum_{i=1}^n Y_i c_{pi}, \quad c_v = \sum_{i=1}^n Y_i c_{vi}, \quad r = \sum_{i=1}^n Y_i r_i = c_p - c_v
\end{aligned} \tag{3}$$

where R is the universal gas constant, T is the temperature, m_i is the molar mass of species i and c_{pi} is the specific heat capacity at constant pressure for species i , which is here expressed in polynomial form as a function of temperature [34]. In this work, the temperature T is found by solving [8]:

$$\rho e = \sum \rho Y_i e_i, \quad e_i := e_{0i} + c_{vi} T \tag{4}$$

where $\rho e = \rho E - \rho \mathbf{v}^2/2$, for each species i , e_{0i} is a constant, and c_{vi} represents the specific heat at constant volume. The total energy per volume for a calorically perfect gas can be written as

$$E_{cal} = e_0 + \frac{p}{\rho(\gamma - 1)} + \frac{|\mathbf{v}|^2}{2} \tag{5}$$

where $\gamma = c_p/c_v$ is the ratio of gas specific heats and e_0 is the reference internal energy at a reference temperature T_0 .

The thermo-viscous-diffusive transport terms, appearing in Equation 2, take the following form:

$$\begin{aligned}
\mathbf{J} &= -\rho \alpha \nabla Y, \\
\tau &= -\frac{2}{3} \mu (\nabla \cdot \mathbf{u}) \mathbf{I} + \mu (\nabla \mathbf{u} + (\nabla \mathbf{u})^T), \\
\mathbf{q} &= -\kappa \nabla T,
\end{aligned} \tag{6}$$

where \mathbf{J} is the species diffusion flux matrix, τ is the viscous stress tensor, described using Newton's law; and \mathbf{q} is the heat-flux vector, modeled using Fourier's law. In these equations, α represents the mixture-averaged species diffusivities, μ is the dynamic viscosity, and κ is the thermal conductivity.

2.1. Entropy pairs and symmetrization of the governing equations

Nonlinear hyperbolic systems of conservation laws arising from physical systems, such as the compressible Euler equations, commonly admit a generalized entropy pair $(U(\mathbf{u}), \mathcal{F}(\mathbf{u}))$ consisting of a convex generalized entropy function $U(\mathbf{u}) : \mathbb{R}^{n_s} \rightarrow \mathbb{R}$ and an entropy flux $\mathcal{F}(\mathbf{u}) : \mathbb{R}^{n_s} \rightarrow \mathbb{R}^d$ that satisfies

$$\frac{\partial \mathcal{F}_j}{\partial u_k} = \frac{\partial F_{ij}}{\partial u_k} \frac{\partial U}{\partial u_i}, \quad i, k = 1, \dots, n_s, \quad j = 1, \dots, d. \quad (7)$$

Entropy pairs exist if and only if the hyperbolic system is symmetrized via the change of variables $\mathbf{v}(\mathbf{u}) = \partial U / \partial \mathbf{u}$ [35, 8], where \mathbf{v} are referred to as the entropy variables. An important property of entropy symmetrized hyperbolic systems emerges when the inner product of the conservation law is taken with respect to the entropy variables, namely, the following identities hold for smooth solutions [36]

$$\mathbf{v}^T \cdot \frac{\partial \mathbf{u}(\mathbf{v})}{\partial t} = \frac{\partial U}{\partial t}, \quad \mathbf{v}^T \cdot (\nabla \cdot \mathbf{F}) = \nabla \cdot \mathcal{F}. \quad (8)$$

We consider the

$$U = -\rho s(\mathbf{u}), \quad \mathcal{F} = -\rho s(\mathbf{u}) \mathbf{v}, \quad (9)$$

where thermodynamic entropy of the mixture, s , is given by:

$$s := \sum_{i=1}^n Y_i s_i, \quad s_i := c_{vi} \ln(T) - \frac{R}{m_i} \ln(\rho Y_i), \quad (10)$$

where s denotes the specific entropy of the mixture, s_i and c_{vi} are the specific entropy and constant volume specific heat for species i , respectively. We note that entropy-satisfying solutions of the Navier-Stokes equation satisfy

$$\frac{\partial U}{\partial t} + \nabla \cdot \mathcal{F} \leq 0 \quad (11)$$

2.2. Mapping of Entropy Variables to Conservative Variables

Using Equation 10 and the Gibbs identity, we can write [8]

$$T d(\rho s) = d(\rho e) - \sum_{i=1}^n g_i d\rho_i = d(\rho E) - \mathbf{v} \cdot d(\rho \mathbf{v}) + \frac{\mathbf{v} \cdot \mathbf{v}}{2} d\rho - \sum_{i=1}^n g_i d\rho_i \quad (12)$$

where g_i is the Gibbs function of species i , so the entropy variables can be written as

$$\mathbf{v}(\mathbf{u}) = \left(\frac{\partial U}{\partial \mathbf{u}} \right) = \frac{1}{T} [g_1 - g_n \quad \cdots \quad g_{n-1} - g_n \quad -g_n - \frac{\mathbf{v} \cdot \mathbf{v}}{2} \quad \mathbf{v} \quad -1]^T, \quad (13)$$

and the entropy potential flux can be derived:

$$\psi(\mathbf{u}) = \mathbf{F}(\mathbf{u})^T \mathbf{v}(\mathbf{u}) - \mathcal{F}. \quad (14)$$

From this expression, using 2, 9, 13, and the relation $\rho_i(e_i - c_{pi}T) = p$ [8], we have

$$\begin{aligned}\psi(\mathbf{u}) &= \frac{1}{T} \left(\sum_{i=1}^{n-1} (g_i - g_n) \rho_i \mathbf{v} + \left(-g_n - \frac{\mathbf{v} \cdot \mathbf{v}}{2} \right) \rho \mathbf{v} + (\rho \mathbf{v} \otimes \mathbf{v} + p \mathbf{I}) \mathbf{v} - (\rho E + p) \mathbf{v} \right) \\ &\quad - \rho s \mathbf{v} = \sum_{i=1}^n c_{pi} \rho_i \mathbf{v} - \frac{e}{T} \rho \mathbf{v} = (c_p - c_v) \rho \mathbf{v} = r(\mathbf{Y}) \rho \mathbf{v}.\end{aligned}\tag{15}$$

Remark 2.1. *In order to derive the mapping from conservative variables to entropy variables, one can first compute the velocity and Gibbs functions as:*

$$v_j = u_{n+j}/u_n, \quad j = 1, \dots, d, \quad g_i = h_i - T s_i = e_i + r_i T - T s_i,\tag{16}$$

where $h_i = e_i + r_i T$ is the specific enthalpy of species i and $r_i = c_{pi} - c_{vi}$. Using these variables and Equation 13, we can obtain entropy variables for multi-component compressible flow.

Remark 2.2. *Likewise, we can transform from the entropy variables to conservative variables by*

$$\mathbf{u} = \left[\rho_1 \quad \dots \quad \rho_{n-1} \quad \rho = \sum_{i=1}^n \rho_i \quad \rho \mathbf{v} \quad \rho c_v T + \frac{(\rho \mathbf{v})^2}{2\rho} \right]^T\tag{17}$$

where, in terms of the entropy variables, we have

$$\begin{aligned}T &= -\frac{1}{v_{n+d+1}}, & v_j &= T v_{n+j}, & j &= 1, \dots, d \\ g_n &= T v_n + \frac{\sum_{j=1}^d v_j^2}{2}, & g_i &= T v_i + g_n, & i &= 1, \dots, n-1, \\ s_i &= c_{pi} - \frac{g_i}{T}, & \rho_i &= \exp\left(\frac{m_i}{R} (c_{vi} \ln(T) - s_i)\right), & i &= 1, \dots, n.\end{aligned}\tag{18}$$

3. Numerical methods

3.1. Finite Volume Discretization

Equation 1 is discretized using the finite volume method. Integrating the governing equation over a control volume V_j and applying the divergence theorem yields:

$$\frac{d}{dt} \int_{V_j} \mathbf{u} dV + \int_{\partial V_j} \mathbf{F} \cdot \mathbf{n} dA - \int_{\partial V_j} \mathbf{G} \cdot \mathbf{n} dA = \int_{V_j} \mathbf{S} dV,\tag{19}$$

where \mathbf{n} is the face normal direction. The volume integrals are approximated as cell-averaged values, and surface integrals are converted to sums over the control volume faces. This results

in the semi-discrete formulation:

$$\frac{d\mathbf{u}_j}{dt} + \frac{1}{V_j} \sum_f (\mathbf{F}_f - \mathbf{G}_f) A_f = \mathbf{S}_j, \quad (20)$$

where \mathbf{F}_f and \mathbf{G}_f represent the face-normal fluxes through face f , A_f is the face area, and V_j is the control volume. The inviscid flux \mathbf{F}_f is computed using a numerical flux function, which depends on the left \mathbf{u}_L and right \mathbf{u}_R states at the face, $\mathbf{F}_f = \mathbf{F}(\mathbf{u}_L, \mathbf{u}_R)$. The viscous flux \mathbf{G}_f depends on the gradients of the conserved variables and is typically computed using central difference approximations.

For time integration, an explicit scheme such as the strong stability-preserving Runge-Kutta (SSP-RK) method [37] is applied. The fully discrete update equation is given by:

$$\mathbf{u}_j^{n+1} = \mathbf{u}_j^n - \frac{\Delta t}{V_j} \sum_f (\mathbf{F}_f - \mathbf{G}_f) A_f + \Delta t \mathbf{S}_j, \quad (21)$$

where Δt is the time step size.

This discretization ensures the conservation of mass, momentum, and energy while accurately resolving fluxes at the interfaces using \mathbf{u}_L and \mathbf{u}_R . In the next subsection, we will discuss the inviscid fluxes based on entropy-conservation and Entropy-Stable methods.

3.2. Entropy-Conservative and Entropy-Stable flux

Writing the Equation 1 for Euler compressible flow, i.e., viscous effects and source term are not considered:

$$\frac{\partial \mathbf{u}}{\partial t} + \nabla \cdot \mathbf{F}(\mathbf{u}) = 0, \quad (22)$$

and multiplying on the left by the entropy variables \mathbf{v}^T , we obtain

$$\frac{\partial U}{\partial t} + \nabla \cdot \mathcal{F} = 0 \quad (23)$$

Thus, the scheme 22 is called *entropy conservative* if it satisfies the Equation 23, and *entropy stable* if it satisfies the inequality

$$\frac{\partial U}{\partial t} + \nabla \cdot \mathcal{F} < 0. \quad (24)$$

In the context of finite volume methods, Tadmor demonstrated how this can be achieved through the judicious choice of numerical flux functions [12]. Tadmor demonstrated that if the flux \mathbf{F}^{ec} satisfies the so-called *shuffle* condition:

$$\llbracket \mathbf{v}(\mathbf{u}) \rrbracket \cdot \mathbf{F}^{ec}(\mathbf{u}_L, \mathbf{u}_R) = \llbracket \psi(\mathbf{u}) \cdot \mathbf{n} \rrbracket \quad (25)$$

where $\llbracket a \rrbracket = a_R - a_L$, then 23 is satisfied and 22 is entropy conservative. Also, The finite volume scheme 22 is entropy stable if the interface flux \mathbf{F}^{es} satisfies an entropy dissipation condition:

$$\llbracket \mathbf{v}(\mathbf{u}) \rrbracket \cdot \mathbf{F}^{es}(\mathbf{u}_L, \mathbf{u}_R) < \llbracket \psi(\mathbf{u}) \cdot \mathbf{n} \rrbracket \quad (26)$$

3.2.1. Kinetic energy preserving with Entropy-Conservative flux

An entropy-conserving flux, defined as

$$\mathbf{F}^{ec} = [\mathbf{f}_{1,1}^{ec}, \dots, \mathbf{f}_{1,N-1}^{ec}, \mathbf{f}_1^{ec}, \mathbf{f}_2^{ec}, \mathbf{f}_3^{ec}],$$

which satisfies condition 25, was introduced in [19, 14, 8]. This flux is given by:

$$\begin{aligned} \mathbf{f}_{1,i}^{ec}(\mathbf{u}_L, \mathbf{u}_R) &= \rho_i^{\ln} \bar{\mathbf{v}} \cdot \mathbf{n}, \quad 1 \leq i \leq n-1, \\ \mathbf{f}_1^{ec}(\mathbf{u}_L, \mathbf{u}_R) &= \sum_{i=1}^n \mathbf{f}_{1,i}^{ec}, \\ \mathbf{f}_2^{ec}(\mathbf{u}_L, \mathbf{u}_R) &= \bar{\mathbf{v}} \mathbf{f}_1^{ec} + p^{ec} \mathbf{n}, \\ \mathbf{f}_3^{ec}(\mathbf{u}_L, \mathbf{u}_R) &= \sum_{i=1}^n \left(e_{0i} + \frac{c_{vi}}{\theta \ln} + \frac{\bar{\mathbf{v}} \cdot \bar{\mathbf{v}}}{2} \right) \mathbf{f}_{1,i}^{ec} + p^{ec} \bar{\mathbf{v}} \cdot \mathbf{n}. \end{aligned} \quad (27)$$

Here, the logarithmic mean is denoted as $a^{\ln} = (a_R - a_L)/(\ln(a_R) - \ln(a_L))$, while the arithmetic mean is given by $\bar{a} = (a_L + a_R)/2$. Additionally, the temperature-related term is defined as $\theta = 1/T$. A robust numerical method for computing a^{\ln} was developed by Ismail and Roe [38]. The interface flux \mathbf{F}^{ec} ensures entropy conservation for the multi-component system defined in Equation 1.

The Entropy-Conserving (EC) flux introduced in this work extends Chandrasekhar's EC flux [14] to a multi-component formulation for the compressible Euler equations. Chandrasekhar's original flux also possesses the Kinetic-Energy Preserving (KEP) property, as described by Jameson [15], a feature particularly advantageous in turbulence simulations [15]. For the compressible Euler equations, Jameson [15] demonstrated that the KEP property is maintained when the momentum flux $f_{\rho u}$ is expressed as

$$f_{\rho u} = p^{ec} + u f_{\rho}, \quad (28)$$

where f_{ρ} represents the mass flux, and p^{ec} is any consistent average of pressure.

Extending Jameson's analysis to a multi-component system follows naturally from [19]. It can be established that the KEP property remains valid when the momentum flux retains the same structural form as in the single-component case, with f_{ρ} representing the total mass flux [19]. The EC flux derived here satisfies these conditions, with p^{ec} given by:

$$p^{ec} = \frac{\sum_{i=1}^n r_i \bar{\rho}_i}{\bar{\theta}}. \quad (29)$$

3.2.2. Entropy-Stable flux

Tadmor [13, 39] introduced a significant class of Entropy-Stable schemes, incorporating an entropy variable-based numerical dissipation term to modify the Entropy-Conservative numerical flux. Starting from EC flux \mathbf{F}^{ec} , we introduce a general numerical dissipation term to obtain a kinetic energy-preserving and Entropy-Stable flux \mathbf{F}^{es} , expressed as

$$\mathbf{F}^{es}(\mathbf{u}_L, \mathbf{u}_R) = \mathbf{F}^{ec}(\mathbf{u}_L, \mathbf{u}_R) - \frac{1}{2} \mathbf{D}(\mathbf{u}_R - \mathbf{u}_L), \quad (30)$$

where \mathbf{D} represents a suitable dissipation operator. To ensure entropy stability, the dissipation term in (30) must be carefully designed so that the numerical flux satisfies the entropy inequality (24). To accomplish this, we redefine the dissipation term to explicitly incorporate the jump in entropy variables:

$$\mathbf{D}(\mathbf{u}_R - \mathbf{u}_L) \simeq \mathbf{D}\mathbf{A}_0(\mathbf{v}_R - \mathbf{v}_L), \quad (31)$$

where $\mathbf{A}_0 = \partial \mathbf{u} / \partial \mathbf{v}$ is the symmetric, positive-definite entropy Jacobian matrix that links the conserved and entropy variables. See Section 2.2 for more details.

3.3. Double-Flux Model

A major challenge in numerical simulations of multi-component flows is the emergence of spurious pressure oscillations, particularly near material interfaces. To identify the root cause and assess the sensitivity of these oscillations, we examine the relationship between internal energy and pressure. This approach was first proposed by Abgrall [29, 40] and later extended to a high-order WENO scheme [5] within the finite difference framework, as well as to a discontinuous Galerkin method [9].

The pressure oscillations arise only for variations in e_0 and γ occurring in multi-component flows. To mitigate them each cell is treated as perfect gas for the convective timestep. To this end, the equivalent perfect gas properties are calculated for each cell as:

$$c_{pi}^* = \frac{\int_{T_0}^T c_{pi}(T) dT}{T}, \quad \gamma^* = \frac{c_p^*}{c_p^* - r} \quad (32)$$

the total energy per unit volume E can be reformulated as

$$\begin{aligned} E &\stackrel{3}{=} \sum_{k=1}^n Y_i (e_{0i} + c_{pi}^* T) - \frac{p}{\rho} + \frac{|\mathbf{v}|^2}{2} \stackrel{32}{=} e_0^* + \sum_{k=1}^n Y_i c_{pi}^* T - \frac{p}{\rho} + \frac{|\mathbf{v}|^2}{2} \\ &= e_0^* + c_p^* T - \frac{p}{\rho} + \frac{|\mathbf{v}|^2}{2} = e_0^* + \frac{p}{\rho(\gamma^* - 1)} + \frac{|\mathbf{v}|^2}{2} \end{aligned} \quad (33)$$

Billet and Abgrall [29] demonstrated that the pressure and velocity of a material interface are preserved if γ^* and ρe_0^* remain constant within each computational cell throughout the entire time step. During reconstruction, these quantities are stored per cell, ensuring

consistency in energy calculations. Based on this approach, the flux at the cell interface $j + 1/2$ is computed twice—once using the e_0^* and γ^* of the left cell and again using those of the right cell. Consequently, the Double-Flux model is inherently non-conservative.

During each stage of the time-marching algorithm the pressure is evaluated from Equation 33. After the timestep the density and pressure are taken from the time-marching scheme. Temperature at the new timestep T^{n+1} is evaluated from the equation of state. Afterwards the caloric equation of state (Equation 5) is evaluated to compute the internal energy at the new timestep and update e_0^* and γ^* .

Remark 3.1. *Without loss of generality, the formulations presented in section 2 can be expressed in terms of γ^* and e_0^* . For instance, the specific heat at constant volume for a general fluid is given by $c_v^* = c_p^* - r$.*

4. Entropy-Stable/Double-Flux scheme

The first subsection presents the necessary preliminaries and notation for developing the Entropy-Stable/Double-Flux scheme. The following subsections focus on the formulation of the numerical flux for the multi-component compressible system.

4.1. Preliminaries and notation

In this subsection, we introduce key mathematical identities and properties that will be used throughout our analysis.

Lemma 4.1. *The jump of the product $r(\mathbf{Y})\rho$ across the interface is equal to the product of r and the jump of ρ across the interface.*

$$\llbracket r(\mathbf{Y})\rho \rrbracket = r\llbracket \rho \rrbracket. \quad (34)$$

Proof. To prove 34, we use the property of the jump operator $\llbracket ab \rrbracket = \bar{a}\llbracket b \rrbracket + \bar{b}\llbracket a \rrbracket$ and $\llbracket r \rrbracket = 0$, so we can expand $\llbracket r(\mathbf{Y})\rho \rrbracket = \bar{r}\llbracket \rho \rrbracket + \bar{\rho}\llbracket r \rrbracket = r\llbracket \rho \rrbracket$. \square

Lemma 4.2. *The term $\sum_{i=1}^n r_i Y_i \llbracket \ln(Y_i) \rrbracket \rho^{\ln}$ is non-positive.*

$$\sum_{i=1}^n r_i Y_i \llbracket \ln(Y_i) \rrbracket \rho^{\ln} \leq 0 \quad (35)$$

Proof. To prove inequality 35, we first use the fact that the sum of the jumps of Y_i across the interface is zero, i.e.,

$$\sum_{i=1}^n \llbracket Y_i \rrbracket = \sum_{i=1}^n Y_{i,R} - \sum_{i=1}^n Y_{i,L} = 1 - 1 = 0. \quad (36)$$

Thus, we can proceed by

$$\sum_{i=1}^n r_i Y_i \llbracket \ln(Y_i) \rrbracket \rho^{\ln} \leq \sum_{i=1}^n \llbracket \ln(Y_i) \rrbracket r \rho^{\ln} = \sum_{i=1}^n \frac{\llbracket Y_i \rrbracket}{Y_i^{\ln}} r \rho^{\ln} \leq \sum_{i=1}^n \llbracket Y_i \rrbracket \frac{r \rho^{\ln}}{Y_i^{\min \ln}} \stackrel{36}{=} 0 \quad (37)$$

where $Y_i^{\min} = \min_{1 \leq Y_i \leq n} Y_i$. \square

Lemma 4.3. *The jump of the product of the inverse temperature and the Gibbs function of species i , is given by:*

$$\llbracket \theta g_i \rrbracket = e_{0i}^* \llbracket \theta \rrbracket + c_{vi}^* \llbracket \ln \theta \rrbracket + r_i \llbracket \ln \rho_i \rrbracket \quad (38)$$

Proof. To prove equation 38, we have

$$\begin{aligned} \llbracket \theta g_i \rrbracket &\stackrel{16}{=} \llbracket \theta(e_i^* + r_i T - T s_i) \rrbracket = \llbracket \theta e_{0i}^* + c_{pi}^* - s_i \rrbracket \\ &\stackrel{10}{=} \llbracket \theta e_{0i}^* + c_{pi}^* + c_{vi}^* \ln \theta + r_i \ln \rho_i \rrbracket = e_{0i}^* \llbracket \theta \rrbracket + c_{vi}^* \llbracket \ln \theta \rrbracket + r_i \llbracket \ln \rho_i \rrbracket \end{aligned} \quad (39)$$

\square

Lemma 4.4. *With consider $\beta = \rho/p = \theta/r$, the following relation holds:*

$$\sum_{i=1}^n \left(e_{0i}^* - \frac{c_{vi}^*}{\theta^{\ln}} \right) Y_i \rho^{\ln} = \left(e_0^* + \frac{1}{(\gamma^* - 1)\beta^{\ln}} \right) \rho^{\ln} \quad (40)$$

Proof. With the observation that $\theta^{\ln} = r \beta^{\ln}$, we get

$$\begin{aligned} \sum_{i=1}^n \left(e_{0i}^* - \frac{c_{vi}^*}{\theta^{\ln}} \right) Y_i \rho^{\ln} &\stackrel{3}{=} \left(e_0^* - \frac{c_v^*}{\theta^{\ln}} \right) \rho^{\ln} = \left(e_0^* - \frac{c_v^*}{r \beta^{\ln}} \right) \rho^{\ln} \\ &= \left(e_0^* + \frac{1}{(\gamma^* - 1)\beta^{\ln}} \right) \rho^{\ln} \end{aligned} \quad (41)$$

\square

4.2. Combine the Entropy-Stable and Double-Flux formulations

In the following, we develop an inviscid numerical flux for the spatial discretization of Equation 1. Our goal is to propose a new type of inviscid numerical flux that is Entropy-Stable and benefits from the advantages of the Double-Flux model. To this end, we first consider the numerical flux \mathbf{F}^{ec} and modify it based on mixture variables. The Entropy-Stable flux for the Double-Flux model $\mathbf{F}^{es*} = [\mathbf{f}_{1,1}^{es*}, \dots, \mathbf{f}_{1,n-1}^{es*}, \mathbf{f}_1^{es*}, \mathbf{f}_2^{es*}, \mathbf{f}_3^{es*}]$ is given by

$$\begin{aligned}
\mathbf{f}_{1,i}^{es*}(\mathbf{u}_L, \mathbf{u}_R) &= Y_i \rho^{\ln} \bar{\mathbf{v}} \cdot \mathbf{n}, \quad 1 \leq i \leq n-1, \\
\mathbf{f}_1^{es*}(\mathbf{u}_L, \mathbf{u}_R) &= \sum_{i=1}^n \mathbf{f}_{1,i}^{es*} = \sum_{i=1}^n Y_i \rho^{\ln} \bar{\mathbf{v}} \cdot \mathbf{n} = \rho^{\ln} \bar{\mathbf{v}} \cdot \mathbf{n} \\
\mathbf{f}_2^{es*}(\mathbf{u}_L, \mathbf{u}_R) &= \bar{\mathbf{v}} \mathbf{f}_1^{es*} + \bar{p} \mathbf{n}, \\
\mathbf{f}_3^{es*}(\mathbf{u}_L, \mathbf{u}_R) &= \left(e_0^* + \frac{1}{(\gamma^* - 1)\beta^{\ln}} + \frac{\bar{\mathbf{v}} \cdot \bar{\mathbf{v}}}{2} \right) \mathbf{f}_1^{es*} + \bar{p} \bar{\mathbf{v}} \cdot \mathbf{n}
\end{aligned} \tag{42}$$

where $\bar{p} = \bar{\rho}/\bar{\beta} = \bar{p\theta}/\bar{\theta}$.

Theorem 4.5. *The finite volume discretization of the multi-component compressible Euler equations with inviscid numerical flux 42 is Entropy-Stable, meaning that the total generalized entropy is non-increasing over time.*

Proof. The flux \mathbf{F}^{es*} is symmetry and consistency follow from symmetry and consistency of the logarithmic mean and average operator. To prove that 42 is Entropy-Stable 26 by following:

$$\llbracket \psi(\mathbf{u}) \cdot \mathbf{n} \rrbracket \stackrel{15}{=} \llbracket r \rho \mathbf{v} \cdot \mathbf{n} \rrbracket \stackrel{3}{=} (\bar{p\theta} \llbracket \mathbf{v} \rrbracket + \llbracket r \rho \rrbracket \bar{\mathbf{v}}) \cdot \mathbf{n} \stackrel{34}{=} \bar{p\theta} \llbracket \mathbf{v} \rrbracket \cdot \mathbf{n} + r \llbracket \rho \rrbracket \bar{\mathbf{v}} \cdot \mathbf{n} \stackrel{3}{=} \bar{p\theta} \llbracket \mathbf{v} \rrbracket \cdot \mathbf{n} + \sum_{i=1}^n Y_i r_i \llbracket \rho \rrbracket \bar{\mathbf{v}} \cdot \mathbf{n} \tag{43}$$

Using short notations for the flux components and the definition of \mathbf{F}^{es*} in 42 we get

$$\begin{aligned}
\llbracket \mathbf{v}(\mathbf{u}) \rrbracket \cdot \mathbf{F}^{es*}(\mathbf{u}_L, \mathbf{u}_R) &= \sum_{i=1}^{n-1} \llbracket \theta(g_i - g_n) \rrbracket \mathbf{f}_{1,i}^{es*} + \llbracket \theta g_n - \frac{\mathbf{v} \cdot \mathbf{v}}{2} \theta \rrbracket \mathbf{f}_1^{es*} + \llbracket \theta \mathbf{v} \rrbracket \cdot \mathbf{f}_2^{es*} - \llbracket \theta \rrbracket \mathbf{f}_3^{es*} \\
&\stackrel{38}{=} \sum_{i=1}^{n-1} ((e_{0i}^* - e_{0n}^*) \llbracket \theta \rrbracket + (c_{vi}^* - c_{vn}^*) \llbracket \ln \theta \rrbracket + r_i \llbracket \ln \rho_i \rrbracket - r_n \llbracket \ln \rho_n \rrbracket) \mathbf{f}_{1,i}^{es*} \\
&\quad + (e_{0n}^* \llbracket \theta \rrbracket + c_{vn}^* \llbracket \ln \theta \rrbracket + r_n \llbracket \ln \rho_n \rrbracket) \mathbf{f}_1^{es*} - \left(\frac{\bar{\mathbf{v}} \cdot \bar{\mathbf{v}}}{2} \llbracket \theta \rrbracket + \bar{\theta} \bar{\mathbf{v}} \cdot \llbracket \mathbf{v} \rrbracket \right) \mathbf{f}_1^{es*} \\
&\quad + (\bar{\theta} \llbracket \mathbf{v} \rrbracket + \bar{\mathbf{v}} \llbracket \theta \rrbracket) \cdot \mathbf{f}_2^{es*} - \llbracket \theta \rrbracket \mathbf{f}_3^{es*} \\
&\stackrel{42}{=} \sum_{i=1}^n (e_{0i}^* \llbracket \theta \rrbracket + c_{vi}^* \llbracket \ln \theta \rrbracket + r_i \llbracket \ln \rho_i \rrbracket) \mathbf{f}_{1,i}^{es*} \\
&\quad - \left(\frac{\bar{\mathbf{v}} \cdot \bar{\mathbf{v}}}{2} \llbracket \theta \rrbracket + \bar{\theta} \bar{\mathbf{v}} \cdot \llbracket \mathbf{v} \rrbracket \right) \mathbf{f}_1^{es*} + (\bar{\theta} \llbracket \mathbf{v} \rrbracket + \bar{\mathbf{v}} \llbracket \theta \rrbracket) \cdot \mathbf{f}_2^{es*} - \llbracket \theta \rrbracket \mathbf{f}_3^{es*}.
\end{aligned} \tag{44}$$

Using Equations 44 and 43 together with the observation that $\llbracket \ln \rho_i \rrbracket = \llbracket \ln Y_i \rrbracket + \llbracket \ln \rho \rrbracket$,

$\llbracket \mathbf{v}(\mathbf{u}) \rrbracket \cdot \mathbf{F}^{es*}(\mathbf{u}_L, \mathbf{u}_R) - \llbracket \boldsymbol{\psi}(\mathbf{u}) \cdot \mathbf{n} \rrbracket$ becomes

$$\begin{aligned} & \sum_{i=1}^n r_i \llbracket \ln \rho \rrbracket (\mathbf{f}_{1,i}^{es*} - Y_i \rho^{\ln} \bar{\mathbf{v}} \cdot \mathbf{n}) + \sum_{i=1}^n r_i \llbracket \ln Y_i \rrbracket \mathbf{f}_{1,i}^{es*} + \bar{\theta} \llbracket \mathbf{v} \rrbracket \cdot \left(\mathbf{f}_2^{es*} - \bar{\mathbf{v}} \cdot \mathbf{f}_1^{es*} - \frac{\bar{p}\bar{\theta}}{\bar{\theta}} \mathbf{n} \right) \\ & + \llbracket \ln \theta \rrbracket \left(\sum_{i=1}^n (e_{0i}^* \theta^{\ln} - c_{vi}^*) \mathbf{f}_{1,i}^{es*} - \theta^{\ln} \left(\mathbf{f}_3^{es*} - \bar{\mathbf{v}} \cdot \mathbf{f}_2^{es*} + \frac{\bar{\mathbf{v}} \cdot \bar{\mathbf{v}}}{2} \mathbf{f}_1^{es*} \right) \right) \end{aligned} \quad (45)$$

inserting \mathbf{F}^{es*} from 42 into 45, and using also Equations 40, 35, so we obtain

$$\llbracket \mathbf{v}(\mathbf{u}) \rrbracket \cdot \mathbf{F}^{es*}(\mathbf{u}_L, \mathbf{u}_R) - \llbracket \boldsymbol{\psi}(\mathbf{u}) \cdot \mathbf{n} \rrbracket = \sum_{i=1}^n r_i Y_i \llbracket \ln(Y_i) \rrbracket \rho^{\ln} \leq 0 \quad (46)$$

which ends the proof and the numerical flux \mathbf{F}^{es*} is Entropy-Stable. Note that for $n = 1$, the numerical flux is entropy-conservative. \square

Remark 4.6. Equation 42 computes the numerical flux more efficiently than Equation 27, requiring only two logarithmic mean evaluations instead of $n+1$. This makes it advantageous for $n > 2$, as logarithmic mean calculations are computationally expensive.

Remark 4.7. It is evident that \mathbf{F}^{es*} satisfies the condition 29. Thus, the numerical flux in Equation 42 is designed to preserve kinetic energy [14].

4.3. Derivation of dissipation at interfaces for Entropy-Stable/Double-Flux method

We here follow the Equation 30 and look for a dissipation of the form 31. Different choices of the dissipation matrix \mathbf{D} yield different numerical fluxes. Two commonly used approaches are the Lax-Friedrichs (LF) [41, 42] and Roe schemes [43]. It is well established that the LF scheme introduces higher numerical dissipation than the Roe scheme. A hybrid dissipation formulation blends these schemes adaptively, applying the more dissipative LF term near strong shocks to enhance robustness while leveraging the less dissipative Roe term in smooth regions and near rarefaction waves or contact discontinuities to improve accuracy. This hybrid dissipation approach is defined as

$$\mathbf{D} = \bar{\mathbf{R}} |\bar{\boldsymbol{\Lambda}}| \bar{\mathbf{R}}^{-1}, \quad (47)$$

where the diagonal matrix of eigenvalues is given by

$$|\bar{\boldsymbol{\Lambda}}| = (1 - \theta) |\bar{\boldsymbol{\Lambda}}| + \theta |\lambda_{max}| \mathbf{I}, \quad \theta = \sqrt{\left| \frac{\llbracket p \rrbracket}{2\bar{p}} \right|} \quad (48)$$

and the parameter $\theta \in [0, 1]$ is defined using a simple local pressure indicator. Here, $\bar{\mathbf{R}}$ is the matrix of right eigenvectors, and $\bar{\boldsymbol{\Lambda}}$ represents the diagonal matrix of eigenvalues of the inviscid flux Jacobian, which is $\bar{\boldsymbol{\Lambda}} = \text{diag}(\bar{v}_n, \dots, \bar{v}_n, \bar{v}_n - \bar{c}, \bar{v}_n, \bar{v}_n, \bar{v}_n, \bar{v}_n + \bar{c})$ and λ_{max} denotes the largest eigenvalue of $\bar{\boldsymbol{\Lambda}}$. Since only the mass flux and energy flux eigenvalues

need to be equal to ensure kinetic energy dissipation [14], we chose eigenvalues of the kinetic energy preserving with Entropy-Stable flux is form

$$\bar{\boldsymbol{\lambda}} = \boldsymbol{\lambda}^{KEPES} = \text{diag}(\bar{v}_n, \dots, \bar{v}_n, \bar{v}_n + \bar{c}, \bar{v}_n, \bar{v}_n, \bar{v}_n, \bar{v}_n + \bar{c}). \quad (49)$$

The average components of the right eigenvectors are given by

$$\bar{\mathbf{R}} = \begin{bmatrix} 1 & \cdots & 0 & Y_1 & Y_1 & 0 & 0 & Y_1 \\ \vdots & \ddots & \vdots & \vdots & \vdots & \vdots & \vdots & \vdots \\ 0 & \cdots & 1 & Y_{n-1} & Y_{n-1} & 0 & 0 & Y_{n-1} \\ 0 & \cdots & 0 & 1 & 1 & 0 & 0 & 1 \\ 0 & \cdots & 0 & \bar{v}_1 - \bar{c} n_x & \bar{v}_1 & -n_y & -n_z & \bar{v}_1 + \bar{c} n_x \\ 0 & \cdots & 0 & \bar{v}_2 - \bar{c} n_y & \bar{v}_2 & n_x & 0 & \bar{v}_2 + \bar{c} n_y \\ 0 & \cdots & 0 & \bar{v}_3 - \bar{c} n_z & \bar{v}_3 & 0 & n_x & \bar{v}_3 + \bar{c} n_z \\ z_1 & \cdots & z_{n-1} & \bar{h} - \bar{c} \bar{v}_n & \frac{1}{2} \|\mathbf{v}_{tot}\|^2 & \bar{v}_2 n_x - \bar{v}_1 n_y & \bar{v}_3 n_x - \bar{v}_1 n_z & \bar{h} + \bar{c} \bar{v}_n \end{bmatrix} \quad (50)$$

where

$$\bar{c} = \sqrt{\frac{\gamma^* \bar{p}}{\rho^{\ln}}}, \quad \bar{h} = e_0^* + \frac{\gamma^*}{\beta^{\ln}(\gamma^* - 1)} + \frac{1}{2} \|\mathbf{v}_{tot}\|^2, \quad \bar{v}_n = \bar{v}_1 n_x + \bar{v}_2 n_y + \bar{v}_3 n_z \quad (51)$$

and $z_i = -\rho^{\ln} \frac{\partial p}{\partial \rho Y_i} / \frac{\partial p}{\partial e}$. The pressure derivatives $\frac{\partial p}{\partial \rho Y_i}$ and $\frac{\partial p}{\partial e}$ are obtained by fixing other variables in the transformed EoS $p = p(\rho, e, \rho Y_1, \dots, \rho Y_{n-1})$.

To construct an Entropy-Stable numerical flux with matrix-based dissipation, a relationship between the entropy Jacobian \mathbf{A}_0 and the right eigenvectors $\bar{\mathbf{R}}$ is required. According to Barth's eigenvector scaling theorem [36], there exists a positive diagonal scaling matrix such that

$$\mathbf{A}_0 = \bar{\mathbf{R}} \bar{\mathbf{T}} \bar{\mathbf{R}}^T \quad (52)$$

where $\bar{\mathbf{T}}$ is defined based on reference [19]. However, the diagonal scaling matrix is defined based on the parameter γ^* , whereas in reference [19], it was originally defined using γ . This modification allows for greater flexibility in adapting the scaling properties to double-flux model while maintaining consistency with the previous approach.

Combining (31), (47), and (52), we express the hybrid dissipation term as

$$\mathbf{D}\mathbf{A}_0(\mathbf{v}_R - \mathbf{v}_L) = \bar{\mathbf{R}} |\bar{\boldsymbol{\lambda}}| \bar{\mathbf{R}}^{-1} (\bar{\mathbf{R}} \bar{\mathbf{T}} \bar{\mathbf{R}}^T)(\mathbf{v}_R - \mathbf{v}_L) = \bar{\mathbf{R}} |\bar{\boldsymbol{\lambda}}| \bar{\mathbf{T}} \bar{\mathbf{R}}^T(\mathbf{v}_R - \mathbf{v}_L). \quad (53)$$

Thus, the Entropy-Stable/Double-Flux flux formulation is given by

$$\mathbf{F}^{es/df}(\mathbf{u}_L, \mathbf{u}_R) = \mathbf{F}^{es*}(\mathbf{u}_L, \mathbf{u}_R) - \frac{1}{2} \bar{\mathbf{R}} |\bar{\boldsymbol{\lambda}}| \bar{\mathbf{T}} \bar{\mathbf{R}}^T(\mathbf{v}_R - \mathbf{v}_L). \quad (54)$$

This formulation guarantees entropy stability by enforcing the entropy inequality in a dis-

crete form. To demonstrate this, we contract the semi-discrete approximation of the multi-component compressible equations with the entropy variables (13). The entropy stability of the flux (54) results in the discrete entropy inequality.

$$\begin{aligned} \frac{\partial U}{\partial t} + \nabla \cdot \mathcal{F} &\leq \llbracket \mathbf{v}(\mathbf{u}) \rrbracket \cdot \mathbf{F}^{es*}(\mathbf{u}_L, \mathbf{u}_R) - \llbracket \boldsymbol{\psi}(\mathbf{u}) \cdot \mathbf{n} \rrbracket \\ &\quad - \frac{1}{2}(\mathbf{v}_R - \mathbf{v}_L)^T \overline{\mathbf{R}} |\overline{\Lambda}| \overline{\mathbf{T}} \overline{\mathbf{R}}^T (\mathbf{v}_R - \mathbf{v}_L) \leq 0 \end{aligned} \quad (55)$$

Since the last term right-hand side of (55) is a quadratic form scaled by a negative factor, the entropy inequality is discretely satisfied.

5. Implementation aspects

This section outlines the implementation of the Entropy-Stable/Double-Flux solver in OpenFOAM, integrating Cantera for chemical kinetics, thermodynamics, transport properties, and Adaptive Mesh Refinement (AMR) for efficiency. The solver employs a density-based approach for accurate shock capturing. AMR enhances computational performance by dynamically refining the mesh based on error criteria. The section also details the high-performance computing setup used for simulations.

5.1. Solver structure

The developed Entropy-Stable/Double-Flux solver is represented by a coupling library implemented in OpenFOAM [44] which connects with the chemical program Cantera [45] and local mesh refinement (AMR) [46]. Density-based solvers are crucial for accurately simulating compressible flows, particularly in scenarios involving strong shocks like those found in turbomachinery. Unlike pressure-based methods, density-based algorithms excel in shock-capturing capabilities, making them the preferred choice for transonic and hypersonic flow calculations. In our work, we adapted the density-based solver from [47] to develop our scheme. Figure 1 shows the schematic structure of the Entropy-Stable/Double-Flux solver.

5.2. Adaptive mesh refinement functionality

With Adaptive mesh refinement (AMR), the local spatial resolution can be dynamically controlled. This allows the maximization of the computational efficiency of the overall simulation as higher resolution is placed only where it is needed. An example grid structure with colored density gradients for the shock-wave and reacting helium gas cylinder interaction problem is shown in Figure2.

For multi-component equation flexibility, AMR's single criterion refinement was extended to multiple different criteria. The criteria include uniquely selected suitable fields and their gradients features such as boxes or domain boundaries as well as the maximum and minimal refinement levels on each individual criterion. The refinement approach proposed by Sun

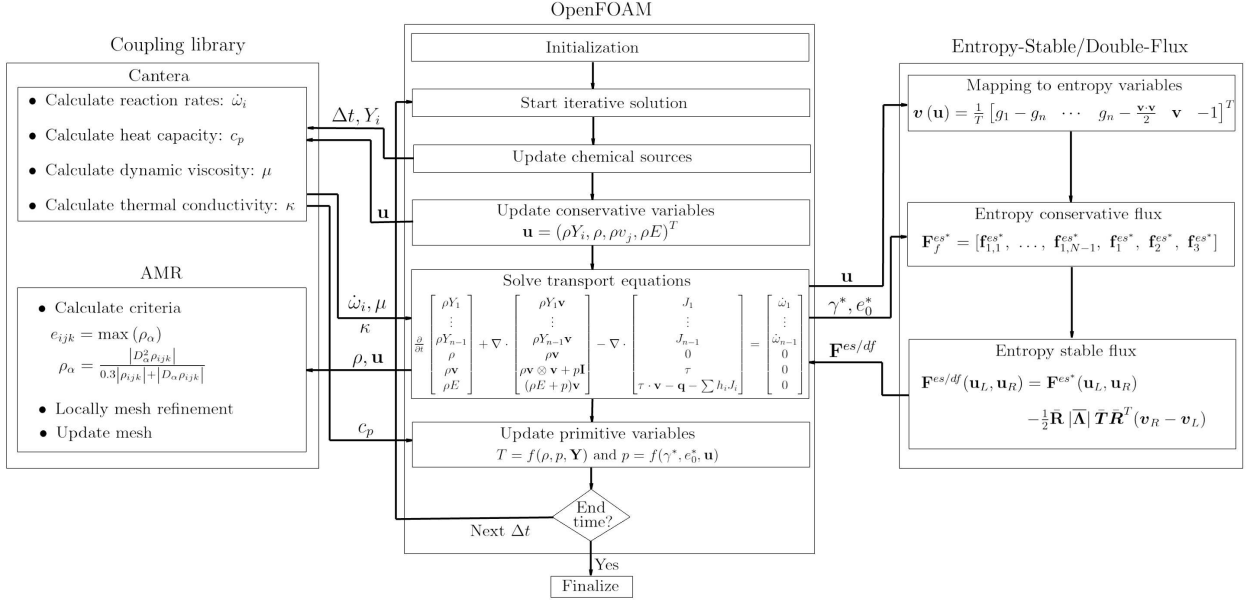


Figure 1: Simplified flowchart illustrating the coupling of the density-based solver in OpenFOAM with Adaptive Mesh Refinement (AMR), the Cantera library, and the Entropy-Stable/Double-Flux solver.

and Takayama [48] is employed to evaluate the maximum error. The error is quantified using a specific metric computed for each cell in a three-dimensional grid, defined as

$$e_{ijk} = \max(\rho_\alpha), \quad \forall \alpha \in \{x, y, z, xy, yx, xz, zx, yz, zy\}, \quad (56)$$

where the error components ρ_α are computed using a general finite-difference stencil:

$$\rho_\alpha = \frac{|D_\alpha^2 \rho_{ijk}|}{0.3|\rho_{ijk}| + |D_\alpha \rho_{ijk}|}, \quad (57)$$

with D_α^2 and D_α representing the second- and first-order finite-difference approximations along the respective directions. The second-order difference is computed as $D_x^2 \rho_{ijk} = \rho_{i-1,j,k} - 2\rho_{i,j,k} + \rho_{i+1,j,k}$, with analogous expressions for other directions. The first-order difference is given by $D_x \rho_{ijk} = \rho_{i+1,j,k} - \rho_{i-1,j,k}$. A block is marked for refinement when the highest error within the block, $e_{\max} = \max(e_{ijk})$, exceeds the refinement threshold $e_{\text{ref}} = 0.1$.

6. Numerical results

In this section, we demonstrate the effectiveness of our Entropy-Stable/Double-Flux approach through a series of test cases with increasing complexity. The goal is to validate the scheme's accuracy and stability across progressively more challenging compressible flow problems. We start with single-component 1D cases 6.1 to establish a baseline, then introduce multi-component 1D problems 6.2 to test the scheme's handling of species interactions. We then extend to multi-component 2D shock-dominated flows 6.3, and finally to a multi-

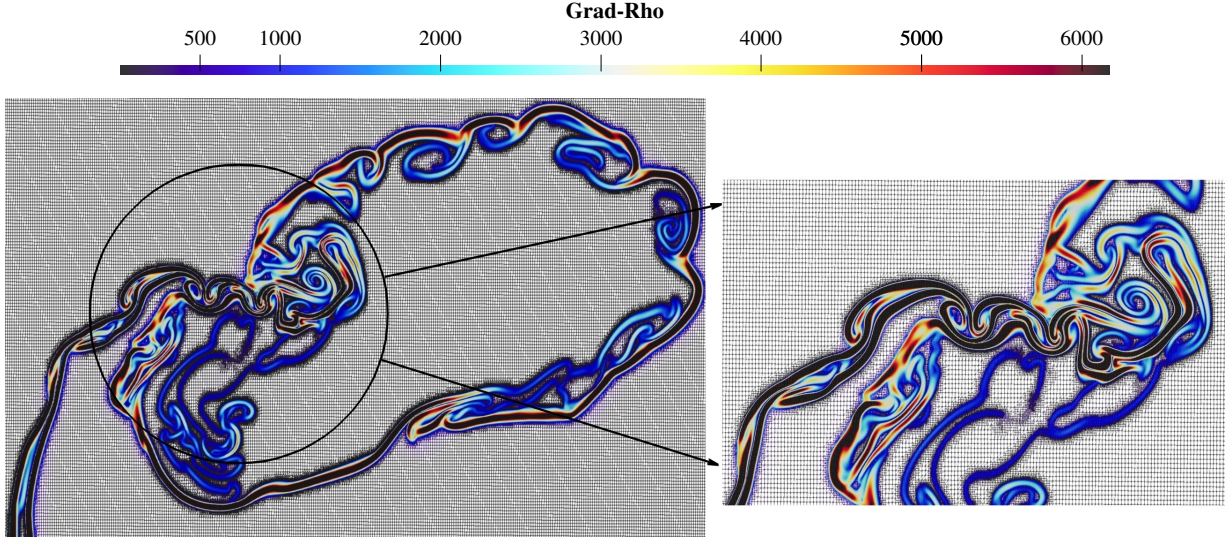


Figure 2: A grid structure with colored density gradients for the shock-wave and reacting helium bubble interaction problem at $t = 700 \mu s$ with three levels of refinement.

component 3D underexpanded jet 6.4, representing a complex, realistic flow scenario¹.

This progression—from 1D to 3D and from single- to multi-component—allows for a clear evaluation of the scheme’s performance under growing numerical and physical challenges.

We use a third-order accurate strong stability preserving Runge-Kutta time integration scheme (SSP-RK3). To ensure numerical stability in a computational run, the time step Δt is determined using the standard finite volume CFL condition:

$$\Delta t = CFL \times \frac{h}{\lambda_{\max}} \quad (58)$$

where h is the characteristic cell length and λ_{\max} represents the maximum wave speed at time step n [49]. The CFL number is a user-defined coefficient that regulates the stability of the simulation. In this study, all computations are performed with $CFL = 0.75$.

6.1. Discontinuous profile on a periodic domain

We examine the discrete evolution of entropy in a single-component test case by evolving a discontinuous initial profile to final time $t = 2s$ on the domain $[-1, 1]$. The initial conditions for density and velocity in non-dimensional form are prescribed as follows:

$$\rho(x, t) = \begin{cases} 3 & |x| < 0.5 \\ 2 & \text{otherwise} \end{cases}, \quad \mathbf{v}(x, t) = 0, \quad p(x, t) = \rho^\gamma. \quad (59)$$

¹Computational experiments were performed on the Lichtenberg II (Phase 1) cluster at TU Darmstadt using multiple nodes, each with dual Intel Xeon Platinum 9242 CPUs (48 cores, 2.3 GHz) and up to 384 GB RAM. The code was compiled with GCC 10.2.0, HWLOC 2.7.1, OpenMPI 4.0.2, and Cantera 3.1.0

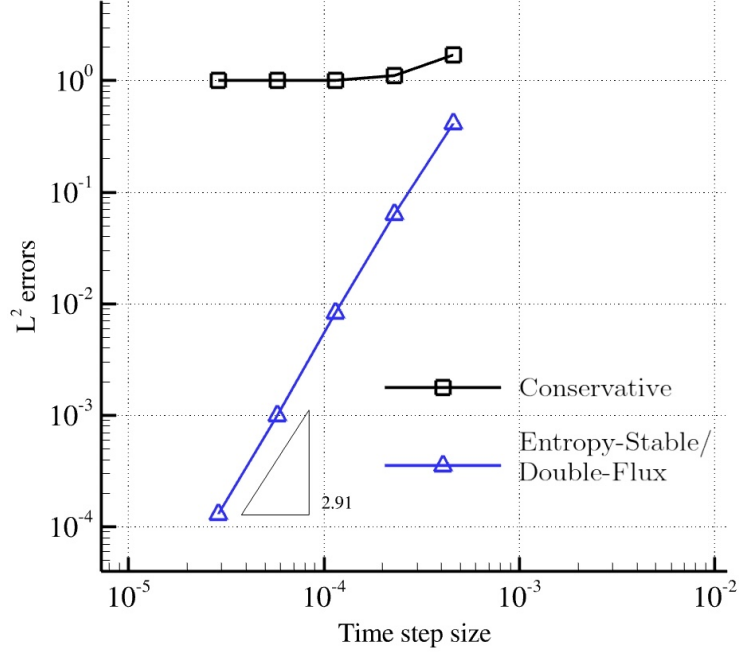


Figure 3: Change in entropy $s(t)$ for both Entropy-Stable/Double-Flux and conservative method using a Lax-Friedrichs (LF) fluxes. The convergence of the change in entropy $s(t)$ at the final time $t = 2s$ converges to zero as $O(\Delta t^{2.91})$ which is the 3rd order time-stepper used.

Periodic boundary conditions are enforced in order to examine the evolution of entropy over longer time periods. The spatial resolution has been fixed to 500. We examine the change in entropy over time. Numerical experiments in [50] suggest that the discrete change in entropy over time should converge to zero as the timestep decreases for Entropy-Conservative flux. We compute the convergence rate of $\Delta s(t) = s(x, t) - s(x, 0)$ to zero with respect to the timestep Δt , as shown in Figure 3.

For this test case, we consider the numerical flux $\mathbf{F}^{es/df} = \mathbf{F}^{es*}$, as defined in Equation 42. To illustrate this, we analyze the flux for a single component ($n = 1$) by setting $Y_1 = 1$ and utilizing Equation 46. This allows us to express

$$\llbracket \mathbf{v}(\mathbf{u}) \rrbracket \cdot \mathbf{F}^{es*}(\mathbf{u}_L, \mathbf{u}_R) - \llbracket \psi(\mathbf{u}) \cdot \mathbf{n} \rrbracket = \sum_{i=1}^n r_i Y_i \llbracket \ln(Y_i) \rrbracket \rho^{\text{ln}} = 0. \quad (60)$$

This result confirms that, for this test case, the numerical flux \mathbf{F}^{es*} is Entropy-Conservative. Furthermore, Figure 3 provides numerical evidence supporting this conclusion.

6.2. Moving interface

The next test problem is the advection of a contact discontinuity (constant velocity and constant pressure) separating two different species. This example illustrates the classic oscillation phenomena when encountering a discontinuous γ with the Entropy-Stable scheme, as well as how this is overcome by the Entropy-Stable/Double-Flux method. Since the

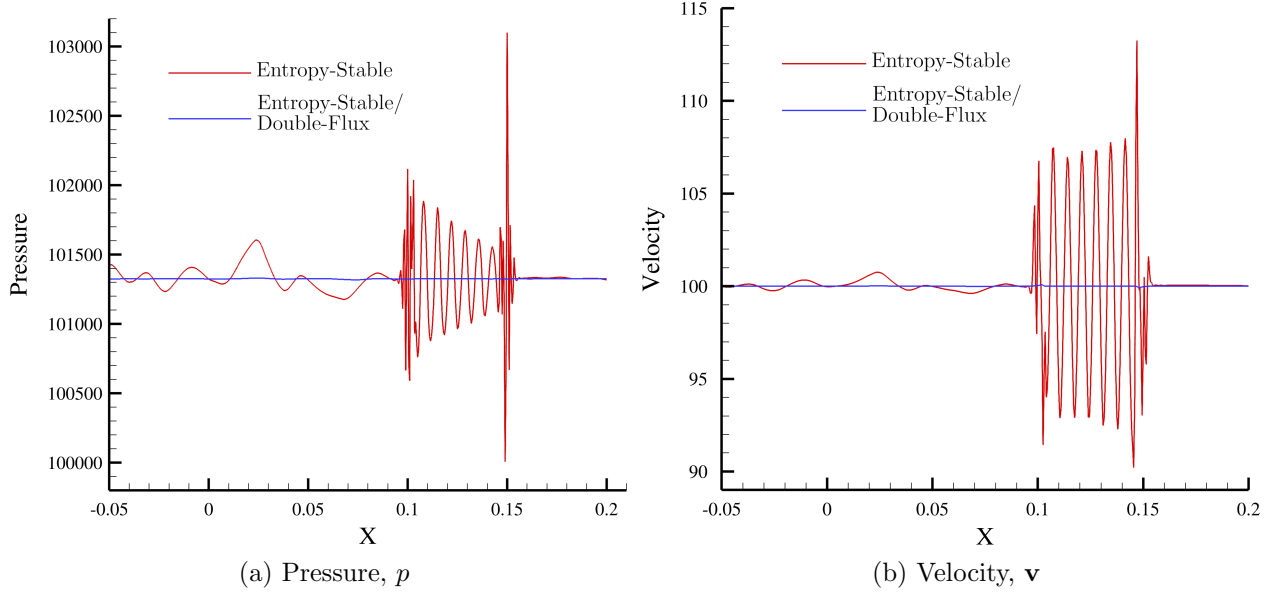


Figure 4: Pressure and velocity profiles for the one-dimensional moving interface problem, $t = 0.001s$.

Double-Flux method is already known to prevent oscillations in this test case [5, 9], we focus on comparing the Entropy-Stable and Entropy-Stable/Double-Flux methods. This highlights the specific effect of the Double-Flux correction when applied within the Entropy-Stable framework. The initial conditions are given by:

$$Y_i(x, t = 0s) = \begin{cases} Y_{H_2} = 1 & 0 \text{ m} < x < 0.05 \text{ m} \\ Y_{N_2} = 1 & \text{otherwise} \end{cases}, \quad \mathbf{v}(x, t = 0s) = 100 \text{ m/s}, \quad (61)$$

$$p(x, t = 0s) = 1 \text{ atm}, \quad T(x, t = 0s) = 300 \text{ K}.$$

The entire domain ranges $[-0.05, 0.5]$ m with 1000 cells and a periodic boundary condition is employed. The pressure and velocity profiles at $t = 0.001s$ are shown in Figure 4.

The observed overshoots and undershoots in the profiles are characteristic of conservative schemes [20] as well as Entropy-Stable methods [15]. These anomalies are inherent to multi-component flows and should be expected. However, the Double-Flux model uniquely maintains accurate pressure and velocity values [51], free from any fluctuations, though this comes at the expense of introducing conservation errors [5]. Notably, the combination of the Entropy-Stable method and the Double-Flux model is shown to accurately capture material interfaces without the occurrence of artificial oscillations. This stability is achieved by freezing the variables γ^* and e_0^* throughout the entire timestep, in conjunction with the Double-Flux algorithm within the Entropy-Stable framework.

6.3. 2D Shock-bubble interaction

This study examines the two-dimensional interaction between a Mach 1.22 shock wave and a helium bubble suspended in air. The experimental configuration, originally investigated by Haas and Sturtevant [52], has been widely used for validating numerical schemes in compressible multiphase flow simulations [6, 53, 54]. The computational domain is defined as $\Omega = (0, 0.325) \text{ m} \times (0, 0.0455) \text{ m}$. Initially, the shock is positioned at $x = 0.225 \text{ m}$, while the helium bubble is centered at $x_0 = 0.175 \text{ m}$. The domain boundaries impose slip-wall and symmetric conditions at the top and centerline, while supersonic inflow and outflow conditions are enforced at the right and left boundaries, respectively. The schematic bubble position and shock-wave location are shown in Figure 5. The initial conditions are summarized in Table 2.

Table 2: Initial conditions for the two-dimensional shock-bubble interaction problem.

Quantity	Pre-shock air	Post-shock air	Helium bubble
ρ [kg/m ³]	1.29	1.7756	0.2347
v_1 [m/s]	0	$(M_2 c_2 - M_1 c_1)$	0
v_2 [m/s]	0	0	0
p [bar]	1	p_2/p_1	1
T [K]	300	$300 T_2/T_1$	300
Y_{N_2}	0.215	0.215	0.000
Y_{O_2}	0.785	0.785	0.000
Y_{He}	0.000	0.000	1.000

where $c = \sqrt{\gamma RT}$ and the normal shock ratios, T_2/T_1 and p_2/p_1 , and post shock Mach number, M_2 , can be calculated from the isentropic flow relations for air $\gamma = 1.4$ which yields, for a $M_1 = 1.22$ normal shock, $T_2/T_1 = 1.14054$, $p_2/p_1 = 1.56979$, and $M_2 = 0.829986$.

Adaptive mesh refinement was used with 1-3 levels of refinement. The computational mesh consists of quadratic elements with three refinement levels $h = (100, 50, 25) \mu\text{m}$. Simulations employ SSP-RK3 to integrate the parabolic terms, with a temporal resolution of $\Delta t = 5 \times 10^{-9} \text{ s}$, corresponding to a maximum CFL number of 0.75 for the finest mesh.

6.3.1. Simulation results and analysis

Figure 6 shows the helium mass fraction images and the density gradients at different times after the shock reached the bubble. At $t = 350 \mu\text{s}$, three key points in the solution are identified as the **downstream**, **jet**, and **upstream** locations, as shown in Figure 6. The **downstream point** corresponds to the leftmost position of the helium bubble, while the **jet point** marks its rightmost position along $y = 0 \text{ m}$. The **upstream point** represents the bubble's farthest right location within the entire domain. When the shock interacts with the helium bubble, these points shift over time, eventually leading to the merging of the jet and downstream locations. The trajectories of these points, depicted in Figure 7 for the Entropy-Stable/Double-Flux scheme with $h = 25 \mu\text{m}$ solution, closely match the solid reference lines from [55].

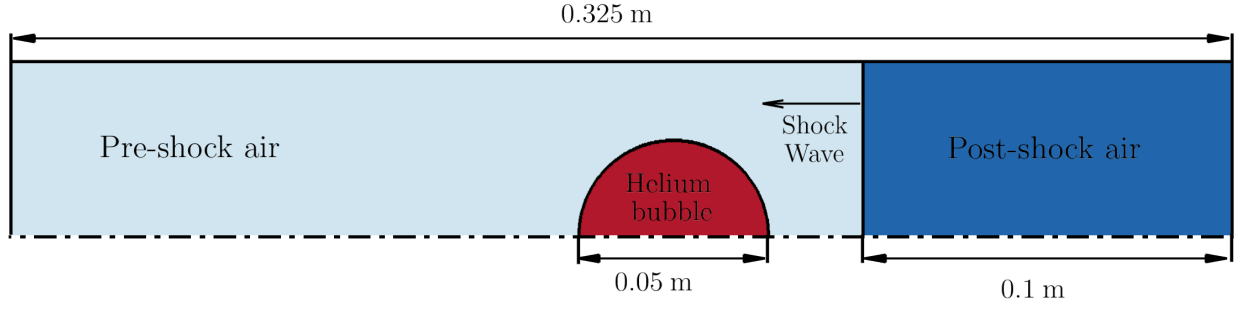


Figure 5: Schematic of the two-dimensional Shock-bubble interaction problem.

The influence of grid resolution on the density gradient at $t = 300, 500$ and $700 \mu\text{s}$ is depicted in Figure 8. Since this test involves fluid instabilities, achieving grid convergence is impossible until the computational cell size becomes significantly smaller than the Kolmogorov scale (approximately $2.5 \mu\text{m}$). This remains impractical to achieve, even when utilizing AMR [5].

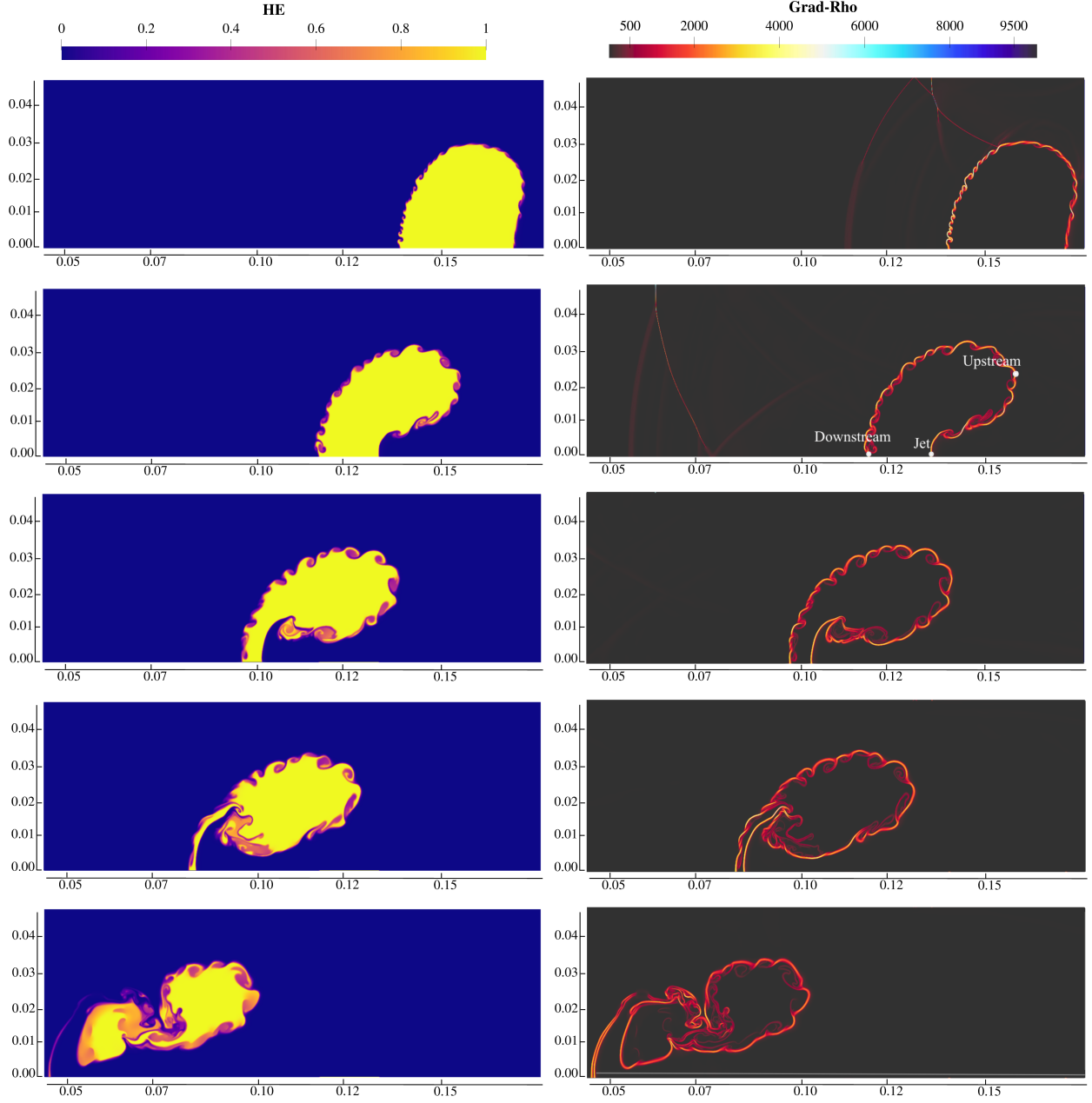


Figure 6: Evolution of helium mass fraction (left) and density gradient magnitude (right) for the interaction with the shock of the helium bubble in air test case computed with the Entropy-Stable/Double-Flux scheme. Time stamps from top to bottom: $t = 200 \mu s$, $t = 350 \mu s$, $t = 500 \mu s$, $t = 600 \mu s$ and $t = 850 \mu s$.

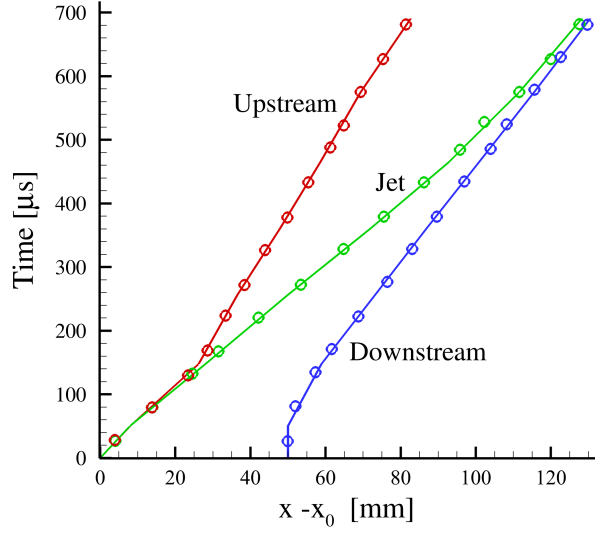


Figure 7: Showing spatiotemporal evolution of characteristics points along the bubble interface from simulations (lines) with $h = 25 \mu\text{m}$ and reported data by Terashima and Tryggvason (symbol circle) [55].

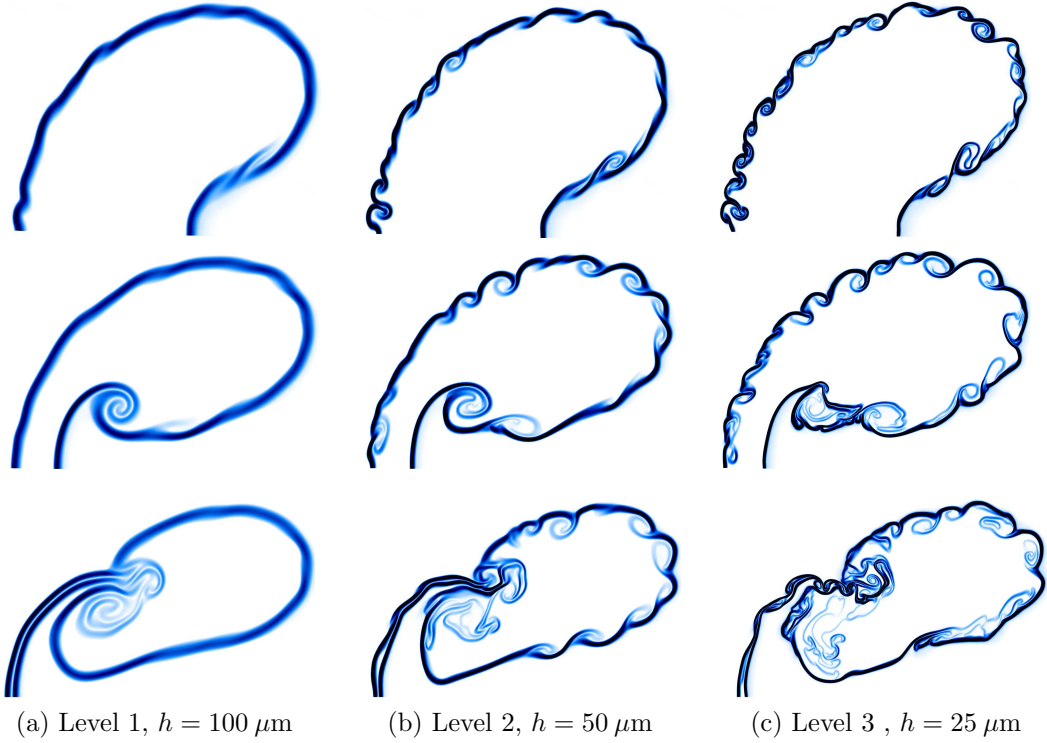


Figure 8: Sequence of local refinements for the two-dimensional Shock-bubble interaction problem. Time stamps from top to bottom: $t = 300 \mu\text{s}$, $t = 500 \mu\text{s}$, and $t = 700 \mu\text{s}$

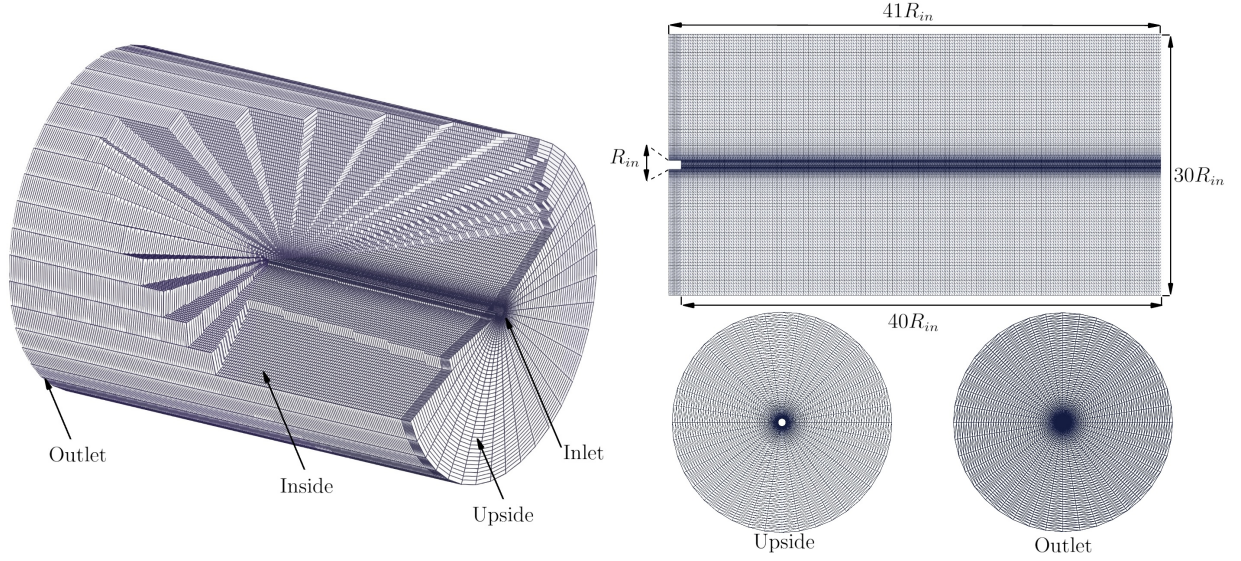


Figure 9: Computational domain for hydrogen injection. The right side presents the setup dimensions, while the left side visualizes a cut through the initial three-dimensional grid structure.

6.4. Under-expanded hydrogen injection

The Entropy-Stable/Double-Flux scheme is evaluated through a supersonic hydrogen jet simulation. Hydrogen's high-pressure injection creates shock waves, impacting fuel-air mixing and combustion. Simulating these flows is complex due to turbulence, acoustics, and shock interactions [56, 57, 58]. To assess the numerical flux scheme's behavior in multi-component jet flows, we adopted a benchmark similar to Hamzehloo et al. [59] and conducted a simulation of an under-expanded hydrogen jet, following the experimental setup of Ruggles and Ekoto [60] with a nozzle pressure ratio (NPR) of 10. The simulation domain is a cylindrical region with a diameter of $30R_{in}$ and a length of $41R_{in}$, where $R_{in} = 1.5$ mm represents the nozzle diameter, see Figure 9.

We simplified the configuration by applying a Dirichlet inlet boundary condition instead of using a high-pressure reservoir. The inlet extends one nozzle diameter into the domain, while Euler slip walls are assigned to the surrounding boundaries, and supersonic outflow conditions are set for the remaining areas. The material parameters used in the three-dimensional under-expanded hydrogen injection simulation are provided in Table 3. The computational domain is structured using a structured hexahedral mesh, consisting of approximately 1.1 million cells at the start of the simulation. As a DNS of this configuration is unfeasible the Smagorinsky eddy viscosity model for the unresolved subgrid contribution is used to run the test case as a large eddy simulation (LES) to investigate the characteristics of hydrogen injection.

6.4.1. Simulation results and analysis

The simulation runs until $t = 55 \mu s$ using $N_{procs} = 3840$ for both the Double-Flux with the HLLC flux function and Entropy-Stable/Double-Flux methods. To achieve higher

Table 3: Initial conditions for the three-dimensional under-expanded Hydrogen injection problem.

Quantity	Inlet	Inside
ρ [kg/m ³]	0.5115	1.1579
v_1 [m/s]	1195.15	0.00
v_2 [m/s]	0	0
v_3 [m/s]	0	0
p [bar]	10	1
T [K]	245.6	296.0
Y_{N_2}	0.000	0.215
Y_{O_2}	0.000	0.785
Y_{H_2}	1.000	0.000

resolution, we applied AMR with a second-layer local refinement, increasing the cell count by 33 million at $t = 55 \mu s$.

The results align well qualitatively with those reported by [59, 60], as evident from the overall flow field comparison. This agreement is further supported by analyzing the position and size of the first Mach disk, as well as the jet penetration for NPR=10 at $t = 55 \mu s$, as presented in Table 4, where a close qualitative match to the data in [59, 60] is observed.

Table 4: Comparison of Mach disk dimensions and penetration depth for different studies and numerical methods in the three-dimensional under-expanded hydrogen injection problem for NPR=10 at $t = 55 \mu s$. AMR1 applies one refinement, while AMR2 applies two.

Author(s)	Mach disk		Penetration [mm]
	Height [mm]	Width [mm]	
Hamzehloo et al. [59]	3.09	1.34	15.80
Ruggles and Ekoto [60]	3.05	1.30	-
Double-Flux, AMR2	3.09	1.36	15.86
Entropy-Stable/Double-Flux, AMR1	3.14	1.38	15.78
Entropy-Stable/Double-Flux, AMR2	3.10	1.32	15.84

The initial transient stages of near-nozzle shock expansion, Mach disk formation, and jet development in the under-expanded hydrogen flow are shown in Figure 10. We can comparing two methods at time $t = 25 \mu s$ and $t = 55 \mu s$. Both methods predict a similar Mach disk position, indicating consistency in capturing the primary shock structures. However, the Entropy-Stable/Double-Flux method reduces numerical dissipation, allowing for a more accurate representation of flow features. In particular, it successfully captures the oblique shock with greater clarity, but with Double-Flux, oblique shock is very diffusive, especially at $t = 25 \mu s$. This behavior is clear for jet boundary and emitted sound in both times.

Hamzehloo et al. [59] demonstrated that mixing occurs before the Mach disk. Where with hydrogen, high levels of momentum exchange and mixing were observed at the boundary

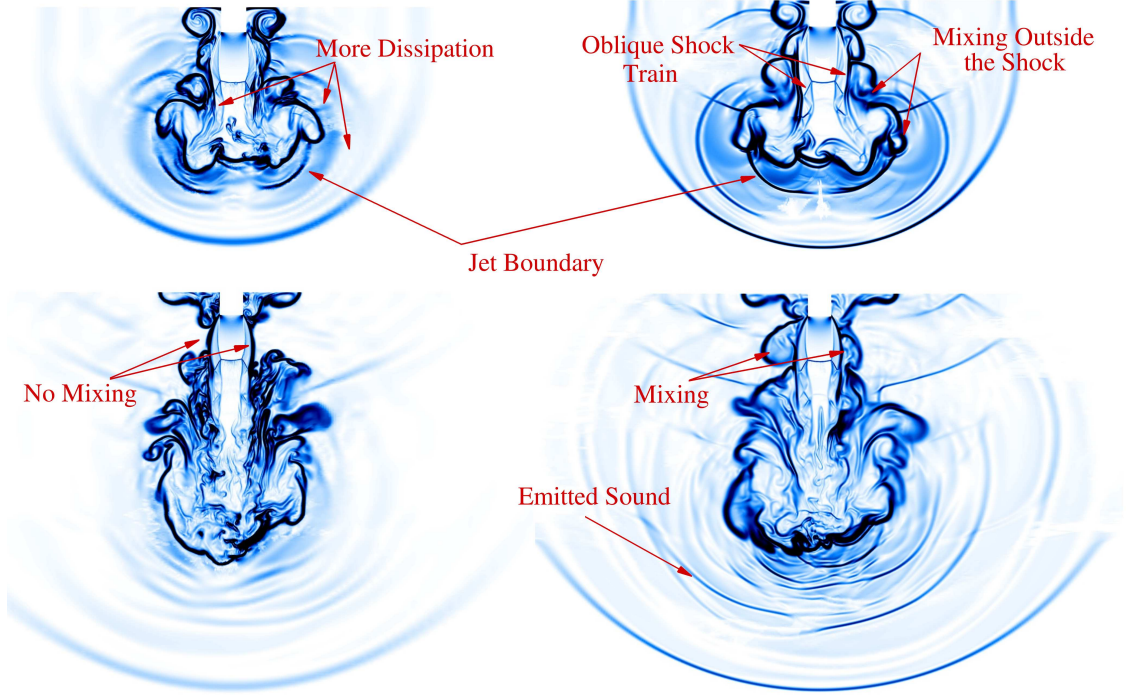


Figure 10: Comparison between the density gradient $|\nabla\rho|$ of the Double-Flux scheme (left) and the Entropy-Stable/Double-Flux method (right). Time stamps from top to bottom: $t = 25 \mu s$ and $t = 55 \mu s$.

of the intercepting shock. The high turbulence fluctuations at the nozzle exit of the hydrogen jet triggered Görtler vortices [59]. As shown in Figure 10, at $t = 55 \mu s$, mixing did not occur before the Mach disk for the Double-Flux method. In contrast, the Entropy-Stable/Double-Flux method exhibited mixing before the Mach disk. For both methods, primary mixing was observed to take place after the Mach disk, particularly near the jet boundaries, where large-scale turbulence played a dominant role [59].

In addition, Figure 11 presents a velocity field slice at $t = 55 \mu s$, comparing both methods. As shown in Figure 11, both methods capture shock waves, consistent with the findings of [59, 60]. However, the Entropy-Stable/Double-Flux method demonstrates greater stability and remains free of oscillations beyond the Mach disk position. This improved stability is attributed to its enforcement of the second law of thermodynamics.

7. Conclusions and future work

This study addresses the numerical challenges associated with simulating multi-component compressible flows that involve strong species mixing, shock interactions, and turbulent dynamics. Such flows often give rise to non-physical oscillations in pressure and temperature due to discontinuities in molar mass and specific heat ratios. Moreover, ensuring consistency with the second law of thermodynamics and maintaining numerical stability in the presence of sharp gradients remains a significant challenge in conventional numerical frameworks.

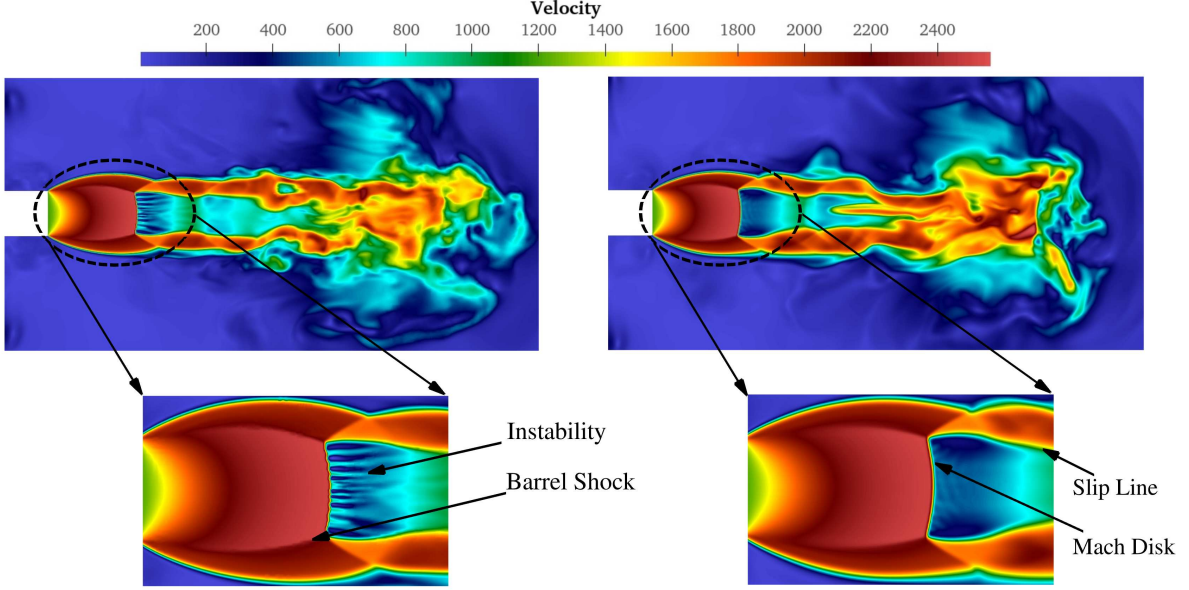


Figure 11: Two-dimension slice of the velocity field for under-expanded hydrogen injection into air at $t = 55 \mu\text{s}$, comparing the Double-Flux scheme (left) and the Entropy-Stable/Double-Flux method (right).

To overcome these limitations, we have developed a new numerical flux formulation that combines the Entropy-Stable method with the Double-Flux approach within a finite volume discretization. This formulation is further enhanced by the inclusion of a hybrid dissipation mechanism, which improves robustness without compromising accuracy. The resulting method ensures entropy consistency, kinetic energy conservation, and oscillation-free behavior across species' interfaces. It also provides enhanced shock-capturing capabilities, particularly in flows with strong compressibility and mixing.

The proposed method was implemented in a density-based solver within the OpenFOAM environment. Its effectiveness was evaluated through a series of progressively challenging test cases designed to assess accuracy, stability, and physical fidelity.

The first test case examines a one-dimensional, single-component isentropic flow with a discontinuous initial profile. In this simplified scenario, the Entropy-Stable/Double-Flux formulation is adapted into an entropy-conserving scheme, demonstrating optimal convergence in entropy variation and confirming the method's theoretical consistency.

The second case considers a two-dimensional, multi-component flow with a moving material interface involving two distinct species. Conventional Entropy-Stable fluxes typically produce spurious oscillations in pressure and velocity at such interfaces. However, the proposed numerical flux successfully eliminates these artifacts, capturing the interface with high fidelity and without introducing non-physical behavior.

The third test case involves a two-dimensional shock–bubble interaction in a multi-component setting. This highly dynamic problem presents strong gradients and interactions between shocks and material interfaces. The Entropy-Stable/Double-Flux scheme closely matches reference solutions and demonstrates improved robustness and numerical stability,

even under severe flow conditions.

In more complex, real-world scenarios, such as the simulation of a supersonic under-expanded hydrogen jet, the method shows an enhanced capability to resolve intricate shock structures, including Mach disks and barrel shocks, while maintaining stability and accuracy downstream of the shock front. Also, the simulation outcomes show strong agreement with both experimental observations and numerical benchmarks from the literature.

In summary, the Entropy-Stable/Double-Flux method offers a significant advancement in the numerical simulation of multi-component compressible flows, especially those involving strong species mixing, shocks, and turbulence. By unifying Entropy-Stable fluxes with Double-Flux mechanisms and augmenting them with a hybrid dissipation model, our method provides a robust, accurate, and thermodynamically consistent framework—paving the way for large-scale simulations, such as LES of turbulent reactive flows, in future work.

CRedit authorship contribution statement

Vahid Badrkhani: Writing – review & editing, Writing – original draft, Visualization, Validation, Software, Methodology, Investigation, Formal analysis, Data curation, Conceptualization. **T. Jeremy P. Karpowski:** Writing – review & editing, Software, Data curation. **Christian Hasse:** Writing – review & editing, Project administration, Funding acquisition, Conceptualization.

Declaration of competing interest

The authors declare that they have no known competing financial interests or personal relationships that could have appeared to influence the work reported in this paper.

Acknowledgements

This work has been funded by the Federal Ministry of Education and Research of the Federal Republic of Germany (BMBF) through the collaborative project CFD4H2, funding reference 03SF0640B, and the German Research Foundation (DFG) – Project no. 349537577.

Data availability

The data that support the findings of this study are available from the corresponding author upon reasonable request.

References

- [1] M. Latini, O. Schilling, W. S. Don, Effects of weno flux reconstruction order and spatial resolution on reshocked two-dimensional richtmyer–meshkov instability, *Journal of Computational Physics* 221 (2) (2007) 805–836.
- [2] S. Kawai, H. Terashima, A high-resolution scheme for compressible multicomponent flows with shock waves, *International journal for numerical methods in fluids* 66 (10) (2011) 1207–1225.
- [3] P. Movahed, E. Johnsen, A solution-adaptive method for efficient compressible multifluid simulations, with application to the richtmyer–meshkov instability, *Journal of Computational Physics* 239 (2013) 166–186.
- [4] S. Vakilipour, M. Mohammadi, V. Badrkhani, S. Ormiston, Developing a physical influence upwind scheme for pressure-based cell-centered finite volume methods, *International Journal for Numerical Methods in Fluids* 89 (1-2) (2019) 43–70.
- [5] R. W. Houim, K. K. Kuo, A low-dissipation and time-accurate method for compressible multi-component flow with variable specific heat ratios, *Journal of Computational Physics* 230 (23) (2011) 8527–8553.
- [6] E. Johnsen, T. Colonius, Implementation of weno schemes in compressible multicomponent flow problems, *Journal of Computational Physics* 219 (2) (2006) 715–732.
- [7] T. Xiong, C.-W. Shu, M. Zhang, Weno scheme with subcell resolution for computing nonconservative euler equations with applications to one-dimensional compressible two-medium flows, *Journal of Scientific Computing* 53 (1) (2012) 222–247.
- [8] F. Renac, Entropy stable, robust and high-order dgsem for the compressible multicomponent euler equations, *Journal of Computational Physics* 445 (2021) 110584.
- [9] Y. Lv, M. Ihme, Discontinuous galerkin method for multicomponent chemically reacting flows and combustion, *Journal of Computational Physics* 270 (2014) 105–137.
- [10] M. T. H. de Frahan, S. Varadan, E. Johnsen, A new limiting procedure for discontinuous galerkin methods applied to compressible multiphase flows with shocks and interfaces, *Journal of Computational Physics* 280 (2015) 489–509.
- [11] E. Gaburro, W. Boscheri, S. Chiocchetti, M. Ricchiuto, Discontinuous galerkin schemes for hyperbolic systems in non-conservative variables: quasi-conservative formulation with subcell finite volume corrections, *Computer Methods in Applied Mechanics and Engineering* 431 (2024) 117311.
- [12] E. Tadmor, The numerical viscosity of entropy stable schemes for systems of conservation laws. i, *Mathematics of Computation* 49 (179) (1987) 91–103.
- [13] E. Tadmor, Entropy stability theory for difference approximations of nonlinear conservation laws and related time-dependent problems, *Acta Numerica* 12 (2003) 451–512.
- [14] P. Chandrashekar, Kinetic energy preserving and entropy stable finite volume schemes for compressible euler and navier-stokes equations, *Communications in Computational Physics* 14 (5) (2013) 1252–1286.
- [15] A. Jameson, Formulation of kinetic energy preserving conservative schemes for gas dynamics and direct numerical simulation of one-dimensional viscous compressible flow in a shock tube using entropy and kinetic energy preserving schemes, *Journal of Scientific Computing* 34 (2008) 188–208.
- [16] P. K. Subbareddy, G. V. Candler, A fully discrete, kinetic energy consistent finite-volume scheme for compressible flows, *Journal of Computational Physics* 228 (5) (2009) 1347–1364.
- [17] G. Coppola, F. Capuano, S. Pirozzoli, L. de Luca, Numerically stable formulations of convective terms for turbulent compressible flows, *Journal of Computational Physics* 382 (2019) 86–104.
- [18] Y. Kuya, K. Totani, S. Kawai, Kinetic energy and entropy preserving schemes for compressible flows by split convective forms, *Journal of Computational Physics* 375 (2018) 823–853.
- [19] A. Gouasmi, K. Duraisamy, S. M. Murman, Formulation of entropy-stable schemes for the multicomponent compressible euler equations, *Computer Methods in Applied Mechanics and Engineering* 363 (2020) 112912.
- [20] R. Abgrall, S. Karni, Computations of compressible multifluids, *Journal of computational physics* 169 (2) (2001) 594–623.

- [21] S. Karni, Multicomponent flow calculations by a consistent primitive algorithm, *Journal of Computational Physics* 112 (1) (1994) 31–43.
- [22] M. J. Castro, U. S. Fjordholm, S. Mishra, C. Parés, Entropy conservative and entropy stable schemes for nonconservative hyperbolic systems, *SIAM Journal on Numerical Analysis* 51 (3) (2013) 1371–1391.
- [23] T. Y. Hou, P. G. LeFloch, Why nonconservative schemes converge to wrong solutions: error analysis, *Mathematics of computation* 62 (206) (1994) 497–530.
- [24] R. Abgrall, S. Karni, A comment on the computation of non-conservative products, *Journal of Computational Physics* 229 (8) (2010) 2759–2763.
- [25] J. Matheis, S. Hickel, Multi-component vapor-liquid equilibrium model for les of high-pressure fuel injection and application to ecn spray a, *International Journal of Multiphase Flow* 99 (2018) 294–311.
- [26] T. Schmitt, L. Selle, A. Ruiz, B. Cuenot, Large-eddy simulation of supercritical-pressure round jets, *AIAA journal* 48 (9) (2010) 2133–2144.
- [27] T. Schmitt, Large-eddy simulations of the mascotte test cases operating at supercritical pressure, *Flow, Turbulence and Combustion* 105 (1) (2020) 159–189.
- [28] H. Terashima, M. Koshi, Approach for simulating gas–liquid-like flows under supercritical pressures using a high-order central differencing scheme, *Journal of Computational Physics* 231 (20) (2012) 6907–6923.
- [29] G. Billet, R. Abgrall, An adaptive shock-capturing algorithm for solving unsteady reactive flows, *Computers & fluids* 32 (10) (2003) 1473–1495.
- [30] P. C. Ma, Y. Lv, M. Ihme, An entropy-stable hybrid scheme for simulations of transcritical real-fluid flows, *Journal of Computational Physics* 340 (2017) 330–357.
- [31] P. C. Ma, H. Wu, D. T. Banuti, M. Ihme, On the numerical behavior of diffuse-interface methods for transcritical real-fluids simulations, *International Journal of Multiphase Flow* 113 (2019) 231–249.
- [32] E. Tadmor, A minimum entropy principle in the gas dynamics equations, *Applied Numerical Mathematics* 2 (3-5) (1986) 211–219.
- [33] X. Zhang, C.-W. Shu, A minimum entropy principle of high order schemes for gas dynamics equations, *Numerische Mathematik* 121 (3) (2012) 545–563.
- [34] B. J. McBride, NASA Glenn coefficients for calculating thermodynamic properties of individual species, National Aeronautics and Space Administration, John H. Glenn Research Center . . . , 2002.
- [35] S. K. Godunov, An interesting class of quasilinear systems, in: *Dokl. Akad. Nauk SSSR*, Vol. 139, 1961, pp. 521–523.
- [36] T. J. Barth, Numerical methods for gasdynamic systems on unstructured meshes, in: *An Introduction to Recent Developments in Theory and Numerics for Conservation Laws: Proceedings of the International School on Theory and Numerics for Conservation Laws*, Freiburg/Littenweiler, October 20–24, 1997, Springer, 1999, pp. 195–285.
- [37] S. Gottlieb, C.-W. Shu, E. Tadmor, Strong stability-preserving high-order time discretization methods, *SIAM review* 43 (1) (2001) 89–112.
- [38] F. Ismail, P. L. Roe, Affordable, entropy-consistent euler flux functions ii: Entropy production at shocks, *Journal of Computational Physics* 228 (15) (2009) 5410–5436.
- [39] U. S. Fjordholm, S. Mishra, E. Tadmor, Arbitrarily high-order accurate entropy stable essentially nonoscillatory schemes for systems of conservation laws, *SIAM Journal on Numerical Analysis* 50 (2) (2012) 544–573.
- [40] R. Abgrall, How to prevent pressure oscillations in multicomponent flow calculations: a quasi conservative approach, *Journal of Computational Physics* 125 (1) (1996) 150–160.
- [41] N. Fleischmann, S. Adami, X. Y. Hu, N. A. Adams, A low dissipation method to cure the grid-aligned shock instability, *Journal of Computational Physics* 401 (2020) 109004.
- [42] V. Badrkhani, R. R. Hiemstra, M. Mika, D. Schillinger, A matrix-free macro-element variant of the hybridized discontinuous galerkin method, *International Journal for Numerical Methods in Engineering* 124 (20) (2023) 4427–4452.
- [43] P. L. Roe, Approximate riemann solvers, parameter vectors, and difference schemes, *Journal of computational physics* 43 (2) (1981) 357–372.

- [44] H. G. Weller, G. Tabor, H. Jasak, C. Fureby, A tensorial approach to computational continuum mechanics using object orientated techniques, *Computers in Physics* 12 (1998) 620–631.
- [45] D. G. Goodwin, *Cantera c++ user’s guide*, California Institute of Technology 32 (2002) 358.
- [46] J. Heylmun, M. E. Fadel, G. Macpherson, J. Hoehler, Openfoam-Com, Luanmingyi, STFS-TUDa/blastAMR: Load-balanced AMR library release, Zenodo (Oct. 2023). doi:10.5281/ZENODO.8427733.
- [47] J. Heylmun, P. Vonk, T. Brewer, blastFoam version 6.0 User Guide (Aug. 2022). URL <https://github.com/synthetic-technologies/blastfoam>
- [48] M. Sun, K. Takayama, Conservative smoothing on an adaptive quadrilateral grid, *Journal of Computational Physics* 150 (1) (1999) 143–180.
- [49] V. Badrkhani, M. F. ten Eikelder, R. R. Hiemstra, D. Schillinger, The matrix-free macro-element hybridized discontinuous galerkin method for steady and unsteady compressible flows, *International Journal for Numerical Methods in Fluids* 97 (4) (2025) 462–483.
- [50] G. J. Gassner, A. R. Winters, D. A. Kopriva, A well balanced and entropy conservative discontinuous galerkin spectral element method for the shallow water equations, *Applied Mathematics and Computation* 272 (2016) 291–308.
- [51] Y. Wang, R. Deiterding, J. Liang, An adaptive solver for accurate simulation of multicomponent shock-interface problems for thermally perfect species, *Computers & Fluids* 291 (2025) 106587.
- [52] J.-F. Haas, B. Sturtevant, Interaction of weak shock waves with cylindrical and spherical gas inhomogeneities, *Journal of Fluid Mechanics* 181 (1987) 41–76.
- [53] A. Marquina, P. Mulet, A flux-split algorithm applied to conservative models for multicomponent compressible flows, *Journal of Computational Physics* 185 (1) (2003) 120–138.
- [54] J. J. Quirk, S. Karni, On the dynamics of a shock–bubble interaction, *Journal of Fluid Mechanics* 318 (1996) 129–163.
- [55] H. Terashima, G. Tryggvason, A front-tracking/ghost-fluid method for fluid interfaces in compressible flows, *Journal of Computational Physics* 228 (11) (2009) 4012–4037.
- [56] S. Crist, D. Glass, P. Sherman, Study of the highly underexpanded sonic jet., *AIAA journal* 4 (1) (1966) 68–71.
- [57] R. S. Snedeker, et al., A study of free jet impingement. part 1. mean properties of free and impinging jets, *Journal of fluid Mechanics* 45 (2) (1971) 281–319.
- [58] V. Vuorinen, J. Yu, S. Tirunagari, O. Kaario, M. Larmi, C. Duwig, B. Boersma, Large-eddy simulation of highly underexpanded transient gas jets, *Physics of Fluids* 25 (1) (2013).
- [59] A. Hamzehloo, P. Aleiferis, Large eddy simulation of highly turbulent under-expanded hydrogen and methane jets for gaseous-fuelled internal combustion engines, *International Journal of Hydrogen Energy* 39 (36) (2014) 21275–21296.
- [60] A. J. Ruggles, I. W. Ekoto, Ignitability and mixing of underexpanded hydrogen jets, *International Journal of Hydrogen Energy* 37 (22) (2012) 17549–17560.